Astronomy & Astrophysics

TANAMI monitoring of Centaurus A: The complex dynamics in the inner parsec of an extragalactic jet[*],[**]

C. Müller[1,2], M. Kadler[2], R. Ojha[3,4,5], M. Perucho[6], C. Großberger[1,2], E. Ros[7,6,8], J. Wilms[1], J. Blanchard[9], M. Böck[7],
B. Carpenter[5], M. Dutka[5], P. G. Edwards[10], H. Hase[11], S. Horiuchi[12], A. Kreikenbohm[1,2], J. E. J. Lovell[13],
A. Markowitz[14,1,15], C. Phillips[10], C. Plötz[11], T. Pursimo[16], J. Quick[17], R. Rothschild[14], R. Schulz[1,2], T. Steinbring[2],
J. Stevens[10], J. Trüstedt[2], and A.K. Tzioumis[10]

(Affiliations can be found after the references)

ABSTRACT

Context. Centaurus A (Cen A) is the closest radio-loud active galactic nucleus. Very Long Baseline Interferometry (VLBI) enables us to study the spectral and kinematic behavior of the radio jet-counterjet system on milliarcsecond scales, providing essential information for jet emission and propagation models.

Aims. In the framework of the TANAMI monitoring, we investigate the kinematics and complex structure of Cen A on subparsec scales. We have been studying the evolution of the central parsec jet structure of Cen A for over 3.5 years. The proper motion analysis of individual jet components allows us to constrain jet formation and propagation and to test the proposed correlation of increased high-energy flux with jet ejection events. Cen A is an exceptional laboratory for such a detailed study because its proximity translates to unrivaled linear resolution, where one milliarcsecond corresponds to 0.018 pc.

Methods. As a target of the southern-hemisphere VLBI monitoring program TANAMI, observations of Cen A are done approximately every six months at 8.4 GHz with the Australian Long Baseline Array (LBA) and associated telescopes in Antarctica, Chile, New Zealand, and South Africa, complemented by quasi-simultaneous 22.3 GHz observations.

Results. The first seven epochs of high-resolution TANAMI VLBI observations at 8.4 GHz of Cen A are presented, resolving the jet on (sub-)milliarcsecond scales. They show a differential motion of the subparsec scale jet with significantly higher component speeds farther downstream where the jet becomes optically thin. We determined apparent component speeds within a range of $0.1\,c$ to $0.3\,c$ and identified long-term stable features. In combination with the jet-to-counterjet ratio, we can constrain the angle to the line of sight to $\theta \sim 12°-45°$.

Conclusions. The high-resolution kinematics are best explained by a spine-sheath structure supported by the downstream acceleration occurring where the jet becomes optically thin. On top of the underlying, continuous flow, TANAMI observations clearly resolve individual jet features. The flow appears to be interrupted by an obstacle causing a local decrease in surface brightness and circumfluent jet behavior. We propose a jet-star interaction scenario to explain this appearance. The comparison of jet ejection times to high X-ray flux phases yields a partial overlap of the onset of the X-ray emission and increasing jet activity, but the limited data do not support a robust correlation.

Key words. galaxies: active – galaxies: individual: Centaurus A – galaxies: individual: NGC 5128 – techniques: high angular resolution – galaxies: jets

1. Introduction

Sample studies of jets of active galactic nuclei (AGN) reveal that the overall jet flow follows a pre-existing channel, and individual components can move at different speeds (e.g., Kellermann et al. 2004; Lister et al. 2009). The kinematics of particular jet features can thus be described with a characteristic speed primarily in the direction of the established jet, although bends and twists can cause changes in the apparent motion vectors or surface brightness due to Doppler boosting. Higher speeds at higher observing frequencies are found (e.g., Jorstad et al. 2001a,b; Kellermann et al. 2004), suggesting that observations at different frequencies sample different parts of the jet. These results can be explained

by a spine-sheath-like structure with a faster inner jet (e.g., Laing et al. 1999; Perucho et al. 2007; Ghisellini et al. 2005; Cohen et al. 2007; Tavecchio & Ghisellini 2008).

Significant acceleration of components has been measured in a number of AGN jets (Homan et al. 2009; Lister et al. 2013) that are both parallel and perpendicular relative to the jet, although it is hard to distinguish whether parallel acceleration is due to a change in the Lorentz factor Γ or a change in the angle to the line of sight. Overall, a positive acceleration trend is found closer to the jet base at ≤ 15 pc, while deceleration occurs farther out. Recent studies by Piner et al. (2012) and Lister et al. (2013) have shown that non-ballistic behavior, i.e., non-radial motion and acceleration, are very common in blazar jets. These authors find a general trend toward increasing speed down the jet for BL Lac objects and radio galaxies and find that orientation effects cannot fully account for these speed changes.

More detailed observations of extragalactic jets at the highest possible resolution are required to study these effects. Centaurus A (Cen A, PKS 1322−428, NGC 5128) presents an

---

ideal target for investigating the innermost regions of AGN to substantiate these proposed explanations. At a distance of only 3.8 Mpc (Harris et al. 2010), the elliptical galaxy Cen A hosts the closest AGN. It exhibits powerful jets, which are observed in the radio and X-ray regimes from subparsec scales up to hundreds of parsecs (Müller et al. 2011; Feain et al. 2011; Hardcastle et al. 2003; Clarke et al. 1992). The morphology of these jets is consistent with Cen A being a Fanaroff-Riley Type I radio galaxy (Fanaroff & Riley 1974). Thanks to Cen A's proximity, the properties of its radio jet can be studied in unprecedented detail on milliarcsecond (mas) scales using Very Long Baseline Interferometry (VLBI), since at this distance an angular size of 1 mas translates into a linear scale of only ∼0.018 pc. The formation and propagation of extragalactic jets is still not completely understood and requires high-resolution information to test and compare them with theoretical models and simulations (e.g., Blandford & Znajek 1977; Blandford & Payne 1982; Vlahakis & Königl 2004; McKinney 2005; McKinney & Blandford 2009; Tchekhovskoy et al. 2011; Fendt et al. 2014).

The time evolution of the mas-scale jet of Cen A has been studied well for over 12 years (1988 to 2000) with VLBI techniques by Tingay et al. (1998, 2001). The jet kinematic has been measured by tracking two prominent components with proper motion $\mu \sim 2$ mas yr^{-1}, corresponding to an apparent velocity $\beta_{app} \sim 0.12$ (where $\beta = v/c$) for the inner mas-scale jet (up to ∼30 mas distance from the core). These observations reveal a stationary component at ∼4 mas distance from the core, with a flux density of ∼0.5 ± 0.3 Jy. Horiuchi et al. (2006) report on a single-epoch space-VLBI observation of Cen A at 5 GHz showing a well-collimated jet, with an intriguingly similar structure to our previously presented results (Müller et al. 2011, hereafter Paper I), which suggests generally stable conditions for the formation and propagation of the jet.

On larger scales, up to 100 pc from the core, Hardcastle et al. (2003) measured a bulk velocity of $\beta_{app} \sim 0.5$ using Very Large Array (VLA) and *Chandra* observations. The presence of radio and X-ray emitting knots could be explained by the interaction of the jet with stars or gas clouds in the host galaxy (Hardcastle et al. 2003; Tingay & Lenc 2009). Worrall et al. (2008) observe a steeper spectrum for components in the outer layers of the jet, which suggests a spine-sheath character for the 100-pc-scale jet.

Hard X-ray observations reveal strong absorption below 2–3 keV, above which the spectrum in the hard X-rays can be modeled with a power law ($\Gamma \sim 1.8$) and narrow fluorescence lines (Evans et al. 2004; Markowitz et al. 2007). Furthermore, observations by Fukazawa et al. (2011) indicate jet emission in this energy band. Tingay et al. (1998) discussed a possible correlation of the increase in X-ray flux with the jet component ejection, although the limited data precluded firm conclusions.

In the framework of the VLBI monitoring program TANAMI (Tracking Active Galactic Nuclei with Milliarcsecond Interferometry, Ojha et al. 2010), Cen A has been monitored at 8.4 GHz and 22.3 GHz approximately twice a year since 2007. We previously presented the first dual-frequency TANAMI observation of this source, which resulted in a very detailed jet image at highest possible linear resolution (Paper I). These images reveal a highly collimated jet at a distance of a few light days from the black hole. The broadband spectral energy distribution (SED) can be described with a single-zone synchrotron/synchrotron self-Compton model (Abdo et al. 2010), though the spectral index distribution of the subparsec scale jet (Paper I) indicates multiple possible emission sites of gamma rays.

A detailed scrutiny of possible high-energy emission processes in Cen A's inner parsec jet system is very important given the suggested positional coincidence of Cen A with ultra-high-energy cosmic rays observed by the Pierre Auger Observatory (e.g., Romero et al. 1996; Honda 2009; Anchordoqui et al. 2001, 2011; Kim 2013). Furthermore, it has recently been shown that the brightest extragalactic jets inside the fields of the first two PeV neutrino events detected by IceCube (IceCube Collaboration 2013; Aartsen et al. 2013) are capable, from a calorimetric point of view, of producing the observed neutrino flux (Krauß et al. 2014). In this context, it is intriguing that Cen A positionally coincides with the recently reported third PeV neutrino event (Aartsen et al. 2014).

Here we report on the evolution of the mas-scale jet structure of Centaurus A at 8.4 GHz. The paper is organized as follows. In Sect. 2 we summarize the observations and data reduction procedure. We then present the high-resolution images at 8.4 GHz in Sect. 3, concentrating on the time evolution of the jet (Sect. 3.3). We discuss these results in Sect. 4 and conclude with an overall picture in Sect. 5.

2. Observations and data reduction

The TANAMI monitoring program (Ojha et al. 2010) has made seven VLBI observations of Cen A at 8.4 GHz between 2007 November and 2011 April. TANAMI uses the Australian Long Baseline Array (LBA) and additional radio telescopes in Antarctica, Chile, New Zealand, and South Africa. Data in the 8.4 GHz band were recorded in single polarization mode with two-bit sampling and correlated on the DiFX software correlator (Deller et al. 2007, 2011) at Curtin University in Perth, Western Australia. They were calibrated using standard procedures in AIPS (Greisen 2003) as described in Ojha et al. (2010). A log of observations and the corresponding image parameters can be found in Table 1. This includes the specific array configuration of each observation, which in general, varies from epoch to epoch. Owing to the contribution of different non-LBA telescopes at different epochs, the (u, v)-coverage, array sensitivity, and angular resolution vary between the different observations. The imaging and self-calibration process of TANAMI data is performed using the CLEAN-algorithm implemented in the program DIFMAP (Shepherd 1997). The major constraint on the image fidelity at 8.4 GHz is the lack of intermediate baselines between the LBA and transoceanic antennas (Paper I). Further details of the TANAMI data reduction and imaging are reported in Ojha et al. (2010) and, specifically for Cen A, in Paper I.

3. Results

3.1. High-resolution imaging

Figures 1 and 2 show the naturally weighted images of the first TANAMI observations at 8.4 GHz with mas resolution. The image parameters and observation characteristics are listed in Table 1. The comparison of the images with different angular resolutions and dynamic ranges (defined as ratio of peak brightness to three times the rms noise level) from ∼500 to ∼1900 allows us to further constrain the position and motion of individual bright jet features.

These images display the jet of Centaurus A in unprecedented detail, clearly resolving particular jet features. The jet-counterjet system is detected in all images and is already well collimated on subparsec scales. We measured a jet opening angle of $\theta \lesssim 12°$ on scales of $\lesssim 0.3$ pc (Paper I).

Table 1. Details of the 8.4 GHz TANAMI observations of Centaurus A.

Obs. date (yyyy-mm-dd)	Array configuration[a]	S_{peak}[b] (Jy beam^{-1})	rms[b] (mJy beam^{-1})	S_{total}[b] (Jy)	$S_{inner\ jet}$[c] (Jy)	b_{maj}[d] (mas)	b_{min}[d] (mas)	PA[d] (°)
2007-11-10	AT-MP-HO-HH-CD-PKS	0.60 ± 0.09	0.40 ± 0.06	2.6 ± 0.4	2.5 ± 0.4	1.64	0.41	7.9
2008-06-09	AT-MP-HO-HH-CD-PKS	1.06 ± 0.16	0.63 ± 0.09	3.1 ± 0.5	2.7 ± 0.4	2.86	1.18	−12.7
2008-11-27	TC-OH-AT-MP-HO-CD-PKS-DSS43	0.74 ± 0.11	0.37 ± 0.06	4.0 ± 0.6	3.1 ± 0.5	0.98	0.59	31.4
2009-09-05	TC-OH-AT-MP-HO-CD-PKS-DSS43	0.76 ± 0.11	0.45 ± 0.07	4.0 ± 0.6	3.0 ± 0.4	2.29	0.58	15.6
2009-12-13	TC-AT-MP-HO-CD-PKS	1.03 ± 0.15	0.18 ± 0.03	3.8 ± 0.6	3.0 ± 0.4	3.33	0.78	26.3
2010-07-24	TC-AT-MP-HO-CD-PKS	1.21 ± 0.18	0.38 ± 0.06	4.2 ± 0.6	3.3 ± 0.5	2.60	0.87	21.4
2011-04-01	TC-WW-AT-MP-HO-HH-CD-PKS-DSS43	0.63 ± 0.09	0.31 ± 0.05	5.1 ± 0.8	3.8 ± 0.6	2.31	0.51	−0.7

Notes. [a] AT: Australia Telescope Compact Array; CD: Ceduna; HH: Hartebeesthoek; HO: Hobart; MP: Mopra; OH: GARS/O'Higgins, PKS: Parkes, TC: TIGO, DSS43: NASA's Deep Space Network Tidbinbilla (70 m); WW: Warkworth; [b] Peak flux density; rms noise level and total flux density in the CLEAN-image; [c] TANAMI 8.4 GHz flux density of inner jet defined by $-2\,\mathrm{mas} \lesssim \mathrm{RA}_{relative} \lesssim 15\,\mathrm{mas}$ and adopting an uncertainty of 15% (see Sect. 4.5); [d] Major and minor axes and position angle of restoring beam.

The jet emission is detected up to a maximum extent of ∼70 mas (≈1.3 pc) from the image phase center and shows an overall straight, well-collimated morphology without any major bends. The counterjet is substantially weaker than the jet at a much lower signal-to-noise ratio. It is as strongly collimated as the jet.

We determine a mean position angle of PA ∼ 50°. The stacked flux density profile along this jet axis (Fig. 3) reveals a declining surface brightness distribution, with resolved individual emission humps.

Assuming an overall calibration uncertainty of 15% (see Paper I for details), the flux density of the inner (∼20 mas) jet shows an increasing trend over the period of observations reported here (∼3.5 years). In particular, we measure a flux density increase of $\Delta S_{inner\ jet} = 1.3 \pm 0.7$ Jy between 2007 and 2011 (see Table 1, Fig. 10 and discussion in Sect. 4.5) in this region.

We identify the VLBI core of the jet at 8.4 GHz as the brightest feature in the map. This result is based on the spectral index imaging in Paper I, as well as on the comparison of individual epochs, i.e., the remarkably similar overall jet structure. The brightest jet knot appears as a pronounced, isolated feature in the stacked profile (see Fig. 3). We assume that it is stationary and considered it to be the 8.4 GHz core.

The second brightest jet feature, an isolated component downstream next to the core at a distance of ∼3.5 mas (see Fig. 3), is found to be stationary with respect to the core (see Sects. 3.3 and 4.2). It most probably corresponds to the stationary component C3 detected by Tingay et al. (2001). Preceding this bright stationary feature (labeled as J_{stat}, see Table A.1 and Fig. 5), i.e., between this component and the core component, a clear decrease in brightness is measured. Figure 3 shows that this dip is also not moving over our monitoring period. However, in epoch 2008.9, an additional component, later associated with J10, is found in this region.

In Paper I we reported on a possible widening and subsequent narrowing of the jet appearing downstream at a distance of ∼25 mas from the core in our 2008 November image. This bifurcation or "tuning fork"-like emission structure around 25.5 ± 2.0 mas is seen in all other 8.4 GHz TANAMI images, although partially masked by the varying uv-coverage in some images. The flux density profile of the stacked image (Fig. 3) illustrates the persistent local flux-density minimum best. It manifests as a remarkably sharp dip in the profile, while most other features are washed out by component motion (see Sect. 4.3). This indicates that the "tuning fork" is a stationary feature in the central-parsec jet of Cen A between 2007 and 2011. The overall jet flux density distribution is declining with

distance and drops where the jet widens. In Sect. 4.3 we discuss the nature of this particular jet structure further.

3.2. Tapered data analysis

The high-resolution TANAMI observations of Cen A are clearly resolving the (sub-)parsec scale jet along and perpendicular to its axis. The overall appearance suggests that we detect substructure in the underlying jet flow.

To test this assumption and to connect our results to previous VLBI studies of the Cen A jet at 8.4 GHz with a ∼(3–15) mas angular resolution (Tingay et al. 1998, 2001), we applied a (u, v)-taper to each dataset, so that the angular resolution compares to previous measurements. As an example, Fig. 4 shows the naturally weighted image at (sub-)mas resolution, as well as the tapered and restored image with comparable resolution to the earlier observations by Tingay et al. (2001). It is obvious that the TANAMI array is resolving small jet substructures, while the main emission zones, which appear as single jet knots in these previous (lower resolution) images, look remarkably similar. This result shows that the observed high-resolution structures are consistent with earlier measurements.

Tingay et al. (2001) discuss the evolution of three individual jet knots C1, C2, and C3. The outer components C1 and C2 have a mean component motion of ∼2 mas yr^{-1}, while C3 appears to be stationary (Tingay et al. 1998, 2001). Adopting the respective reported apparent motions and uncertainties, we can determine their expected positions at the time of our TANAMI observations. Figure 4 shows that these extrapolated positions match well with prominent emission regions in the tapered TANAMI image within the uncertainties given by the velocity measurement by Tingay et al. (2001). We can therefore associate these components with features detected in the TANAMI images (see Sect. 3.3). This comparison is further discussed in Sect. 4.

3.3. Time evolution of the mas-scale jet

The high spatial resolution and the good sampling of the TANAMI monitoring of Cen A at 8.4 GHz allow us to study the time evolution of the closest extragalactic jet in unprecented detail. To parametrize individual jet features and to track their evolution with time, we fit Gaussian emission model components to the self-calibrated visibility data (see Sect. 3.1) using the modelfit task in DIFMAP (Shepherd 1997). The best-fit parameters for each TANAMI 8.4 GHz observation of Cen A are listed in Table A.1. The identified jet components, which can be tracked over several epochs, are explicitly labeled. The models
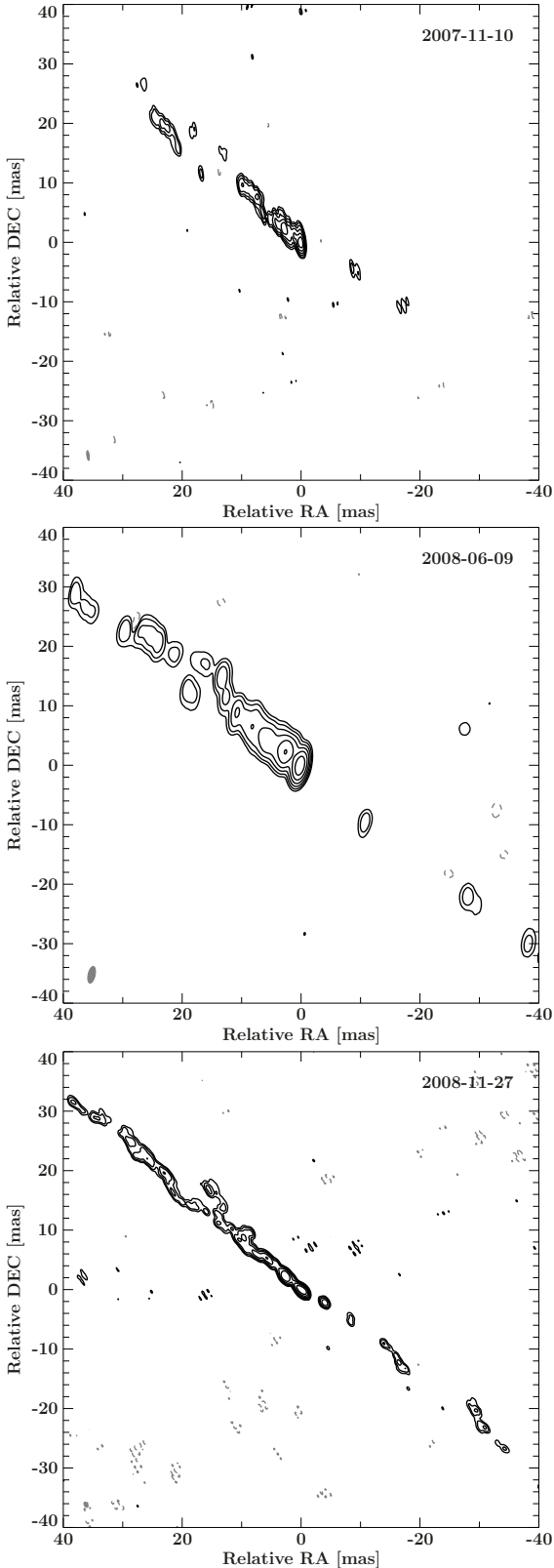
Fig. 1. Contour images of the first three 8.4 GHz TANAMI observations with natural weighting. The black contours indicate the flux density level, scaled logarithmically and increased by a factor of 3, with the lowest level set to the 3σ-noise-level (for more details see Table 1). Negative contours are shown in gray. *From top to bottom*: 2007 November (Ojha et al. 2010), 2008 June, 2008 November (Paper I). The FWHM of the restoring beams for each observation is shown as a gray ellipse in the lower left corner. 1 mas in the image corresponds to 0.018 pc.

for every single epoch were constructed following the same procedure. The self-calibrated visibility data were fit with sufficient Gaussian model components to describe the prominent bright jet features, leading to final models with $\chi^2 \sim 2232$ (d.o.f. = 2350)[1] to $\sim$23 906 (d.o.f. = 6846, see Table A.1). Figure 5 summarizes the result of the kinematic study showing the contour images overlaid by the corresponding Gaussian model components[2]. The brightest upstream feature, identified as the core (see Sect. 3.1), was taken as a reference position and all positions are measured with respect to it.

We performed a statistical error calculation for the model fit parameters by interfacing DIFMAP with the data-reduction package ISIS (Houck & Denicola 2000). This approach allows us to use the functionality contained in this general purpose system to efficiently determine the parameter values and their uncertainties based on the χ^2 statistics. The error calculation was performed for each parameter. We find that the systematic uncertainties dominate (typically by more than an order of magnitude) over the statistical errors even if cross-coupling between adjacent components is considered. Therefore, we adopt the semi-major component axis as an estimate of positional uncertainties of individual emission features and conservatively estimated 15% calibration uncertainties (see Paper I) for component flux densities.

We can identify multiple individual components besides the core (Fig. 6), labeled J1 to J10 and J_{stat} (see Table A.1). One component is found to be stationary (J_{stat}). It shows remarkably constant brightness temperature behavior. For the analysis of the time evolution of the components, we excluded the whole region of the jet widening (Sect. 3.1), since cross-identification of related edge-components suffers from larger positional uncertainties and larger offsets to the jet axis. The position of the "tuning fork" like emission with lower surface brightness remains stationary, as clearly seen in the stacked flux density profile (Fig. 3).

Seven of the moving components are detected in more than four consecutive epochs. Two newly emerged components (J10 and J9) are ejected into the jet during the TANAMI monitoring period. Component J10 could only be detected in three epochs so far and further VLBI observations are required to better constrain its trajectory (see below). The two outermost components J2 and J1 only appear in two data sets because of limited short-baseline (u, v)-coverage and sensitivity in some epochs. The study of the jet kinematics of Cen A will be discussed based on the time evolution of the components J3 to J10.

Assuming ballistic motion for each component, we determine the individual apparent speeds for the components J3 to J10 using linear regression fits to the centroid position of associated Gaussians. This is the most solid approach because testing for possible acceleration of single components is not reliable until robust detection of components in more than ten consecutive epochs, as discussed in (Lister et al. 2013). We detect a clear velocity dispersion (see Table 2). The individual component proper motions range from $\mu = 1.78 \pm 0.19$ mas yr^{-1} for J8 to $\mu = 4.98 \pm 0.38$ mas yr^{-1} for J3. The mean apparent speed of these eight components is $\mu_{mean} = 2.98$ mas yr^{-1}, and the median is $\mu_{median} = 2.83$ mas yr^{-1}. This shows a broader range of speeds for the different resolved components than the values determined by Tingay et al. (2001). The tapered data can explain this discrepancy. As discussed in Sect. 3.2, the comparison of the

---

[1] The number of degrees of freedom is determined as the number of real and imaginary part of complex visibilities minus the number of free model parameters.

[2] Owing to the lower signal-to-noise ratio of the counterjet, no kinematic measurements could be obtained.
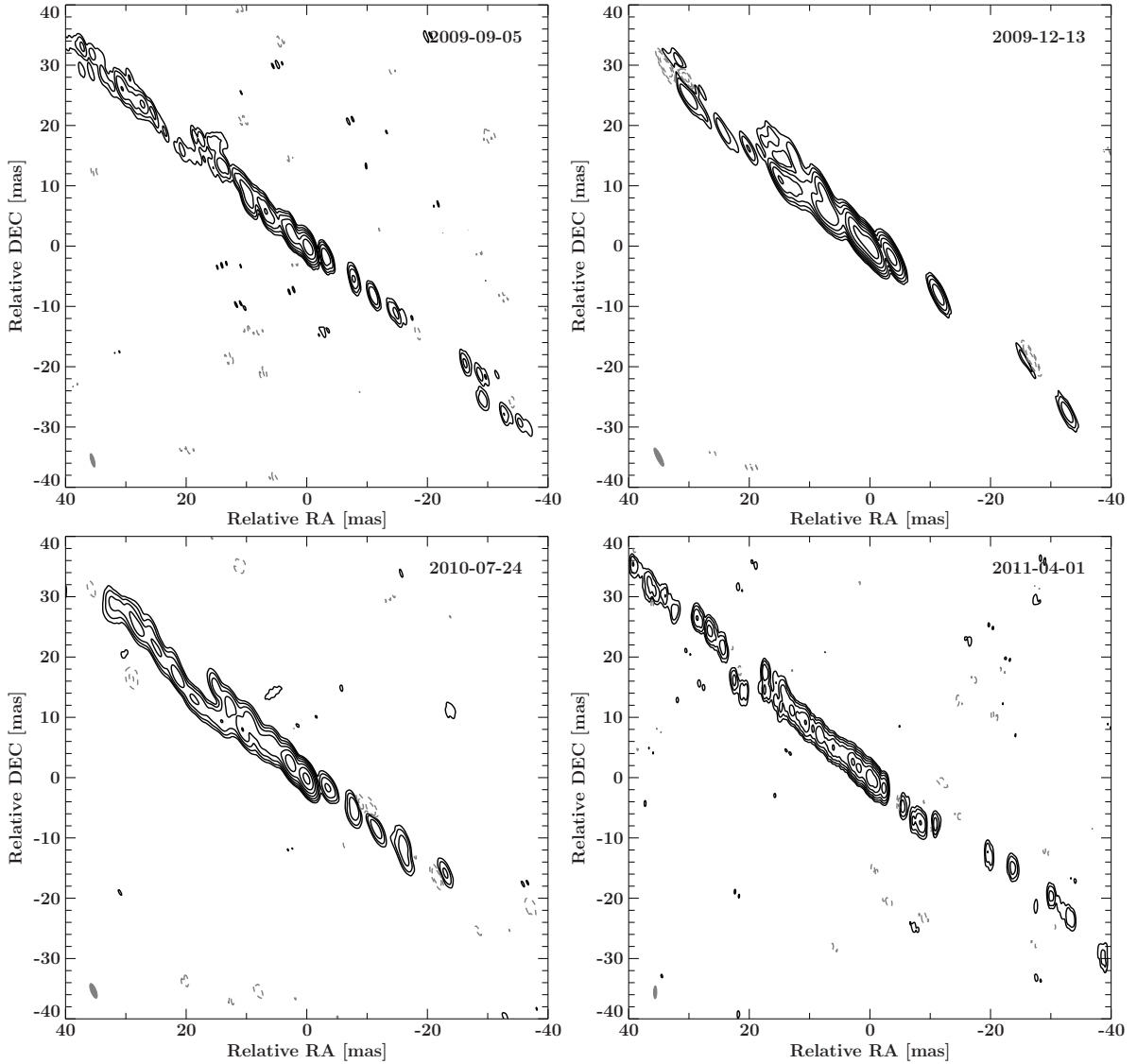
Fig. 2. Same as Fig. 1 for the 4th to 7th TANAMI observations. From *top left to bottom right*: 2009 September, 2009 December, 2010 July, and 2011 April.

Table 2. Apparent speeds of individual jet components.

ID	μ [mas/yr]	β_{app}	d_{mean} [mas][a]	$t_{ejection}$
J3	4.98 ± 0.38	0.29 ± 0.02	53.96	$\sim 1983^{b}$
J4	3.98 ± 0.23	0.23 ± 0.01	38.89	$\sim 1989^{b}$
J5	2.85 ± 0.13	0.17 ± 0.01	34.47	$\sim 1989^{b}$
J6	3.16 ± 0.10	0.19 ± 0.01	18.67	2002.0 ± 1.0
J7	1.82 ± 0.25	0.11 ± 0.01	13.76	2002.0 ± 2.0
J8	1.78 ± 0.17	0.10 ± 0.01	9.60	2005.0 ± 1.0
J9	2.47 ± 0.13	0.15 ± 0.01	5.90	2007.5 ± 0.5
J10	2.83 ± 0.14	0.17 ± 0.01	4.27	2008.5 ± 0.5

Notes. [a] Mean component distance from the core. Note that the time range over which single components have been tracked is shorter for the two newly emerged components J9 and J10. [b] Results from Tingay et al. (2001), see main text for details.

tapered TANAMI images with these previous observations and the extrapolation of the component position to the time of the TANAMI observations (see Figs. 4 and 7) allows us to identify the component complex J5 to J3 with components C2 and C1 of Tingay et al. (2001), respectively (see Sect. 4 for further details).

We can therefore conclude that the larger scale structure, shown in the tapered images, moves with a mean speed comparable to the results by Tingay et al. (2001). This comparison shows the influence of limited angular resolution in Cen A kinematic studies. Higher resolution TANAMI observations allow us to detect small-scale structures that seem to follow a pre-existing channel defined by the flow, but show distinct apparent speeds.

Assuming constant component velocities and no intrinsic acceleration, the back-extrapolation of the component tracks constrains the ejection times for the innermost components (see Table 2). The ejection times of J5 to J3 are obtained using the tapered analysis and the cross-identification with C2 ($1989.2^{+0.9}_{-0.7}$) and C1 ($1983.5^{+2.2}_{-3.2}$) from Tingay et al. (2001).

Figure 8 shows the β_{app}-distribution for each component as a function of mean distance from the core. The pc-scale jet of Cen A shows a trend toward an increasing component velocity farther downstream, which can be parameterized by a linear fit of $\beta_{app} = 0.16\,d + 0.11$, where d is the mean component distance in pc over the observed time range. Components J4 and J3 show significantly higher speeds than components closer to the core, suggesting that the jet undergoes acceleration farther out, as seen in a statistically large sample of AGN jets by Lister et al. (2013).
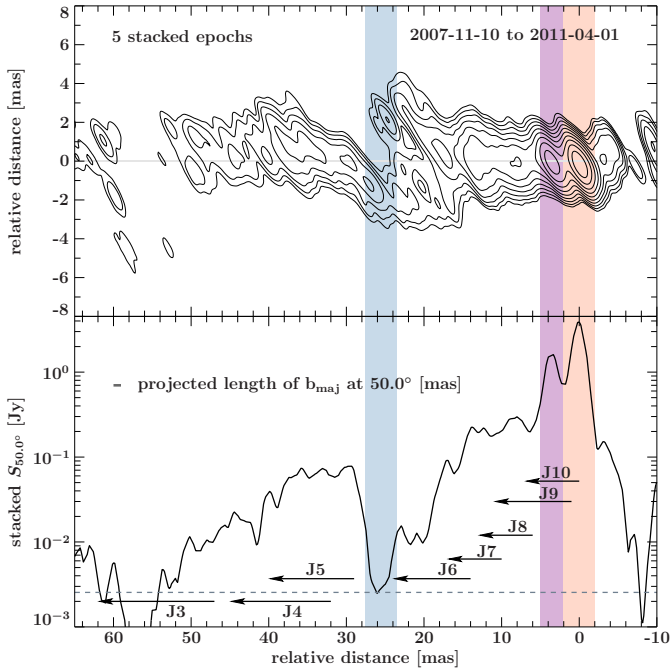
Fig. 3. *Top*: stacked CLEAN image. The five highest resolution TANAMI images (epoch 2007.86, 2008.9, 2009.68, 2010.56, 2011.25) were restored with a common beam of size (2.29×0.58) mas at PA = $15.6°$ and rotated by $40°$. *Bottom*: flux density profile along the jet axis (at PA = $50°$) of stacked 8.4 GHz CLEAN images. The gray dashed line indicates the noise level of the stacked image. The orange and purple shaded areas mark the core region and the stationary component, respectively. The blue shaded area at 25.5 ± 2.0 mas away from the phase center indicates the region of the jet where the widening and decrease in surface brightness at 8 GHz occurs. The projection of the restoring beam width onto the jet axis is shown as a gray line. The black arrows indicate the traveled distances of the identified components causing a smoothing of the profile due to the jet flow with $\mu_{mean} \sim (2-3)\,\mathrm{mas\,yr}^{-1}$ (see Sect. 3.3 and compare to Tingay et al. 2001).

The best-fit apparent velocities of the two newly emerged components J9 and J10 agree within their errors, but deviate from the mean jet speed. Both components pass the stationary feature during the time of TANAMI monitoring, a very complex region where misidentification is possible. They are faster than the more robust components J7 and J8. More VLBI observations will be able to test the higher speeds of J9 and J10.

3.4. Simultaneous ballistic fit

The characterization of the jet flow with ballistic tracks is a good approach to determine the motion of the individual components. However, the motion tracks could in principle be more complex. In the following we introduce a method that fits all data sets for all epochs simultaneously with the constraint that component trajectories have to follow ballistic tracks. We couple the positions of all components in the individual epochs using a single linear model and then solve for all component velocities by performing a simultaneous fit to all epochs. As a starting model, to identify the components we use the models obtained for each single (u, v)-dataset. When assuming ballistic motion, the time evolution of each identified component i (with $i = 1 \ldots 10$) can then be described by

$$x = x_{0,i} + \cos(\phi_i)v_i(t - t_{0,i})$$
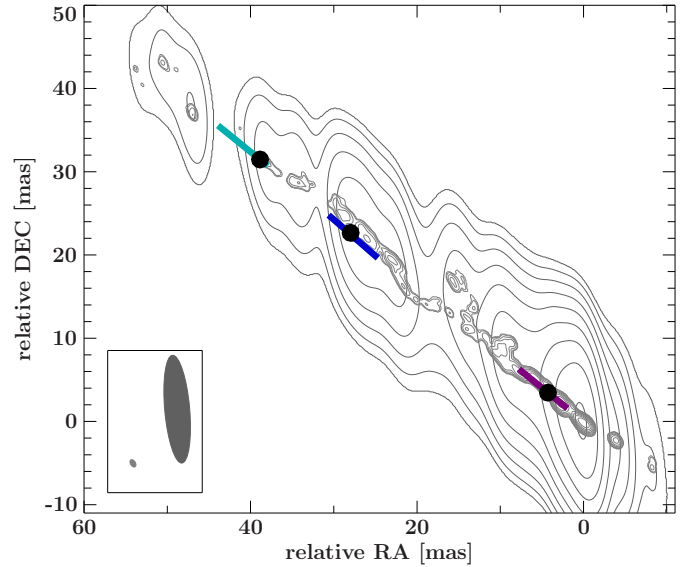$$y = y_{0,i} + \sin(\phi_i)v_i(t - t_{0,i}) \qquad (1)$$

Fig. 4. Tapered (dark gray) and original 2008 November TANAMI image (light gray). A taper of 0.1 at $25\,M\lambda$ was chosen and the image was restored with the common beam of (3×13) mas at $5°$ as applied in Tingay et al. (2001) in order to compare the TANAMI observations with these previous VLBI measurements. In the lower left the size of the respective restoring beam is shown as a gray/black ellipse. The tapered TANAMI image is remarkably similar to the images by Tingay et al. (1998, 2001). The extrapolation of the motions of the components monitored by Tingay et al. (2001), adopting the respective measured apparent speed for each of the three components C1, C2, and C3, results in hypothetical component positions for this observation. The black filled circles indicate these expected positions, the purple/blue/cyan lines represent the positional uncertainties of C3/C2/C3 derived from the velocity error. This comparison shows that TANAMI observations are consistent with previous results.

where (x_0, y_0) is the the starting position, ϕ_i is the ejection angle, $t_{0,i}$ the ejection date, and v_i the velocity. Based on this input model we performed a simultaneous fit to all datasets by fitting ballistic motion to all identified components, resulting in a combined χ^2. As a consequence of this approach, if the motion is non-ballistic, the fit will result in a high χ^2-value, so that we can reject the hypothesis of simple ballistic motion.

This approach results in a $\chi^2 = 74\,149$ with $39\,044$ degrees of freedom ($\chi^2_{red} = 1.9$) for the combined, simultaneous fit. The resulting component velocities agree with the values obtained by the single fits using the "classical" approach (see Sect. 3.3). We conclude that the motion of the identified components are described well by ballistic motion on the basis of seven consecutive observations, though the best-fit has only a moderate χ^2_{red}-value. The downstream acceleration is confirmed by this analysis, with $\sim 1-2\,\mathrm{mas\,yr}^{-1}$ faster speeds for J5 to J3 than for the inner components. We expect that with further monitoring epochs, this analysis will yield a good test of a continuous acceleration model along the jet.

4. Discussion

In the following sections we discuss the Cen A jet kinematics. On top of the overall jet flow, the series of highly resolved images of Cen A reveal particular bright and interestingly shaped structures, which are discussed in detail.
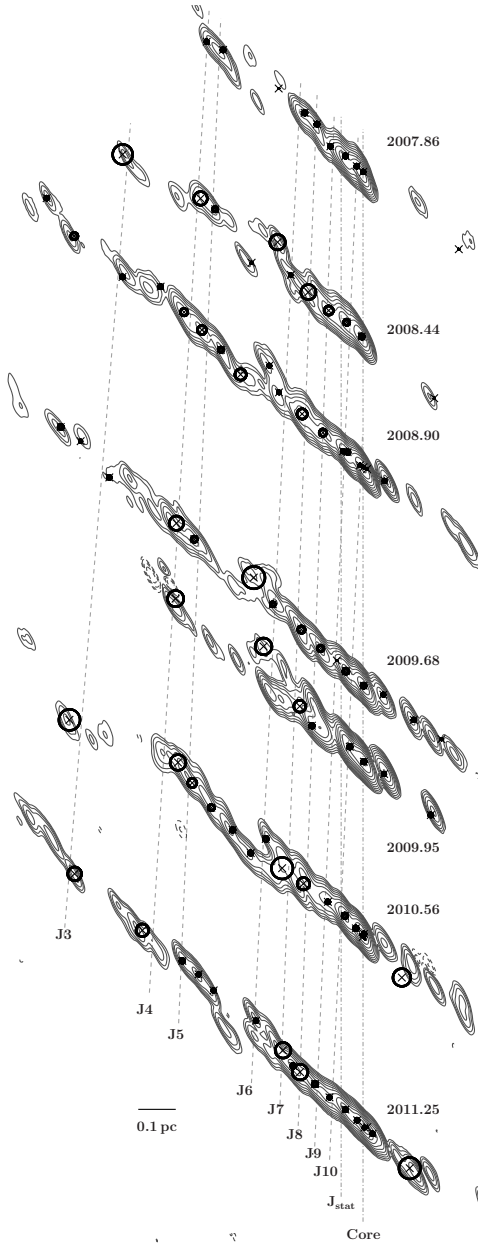
Fig. 6. Component distance from the core component (set to zero) as a function of time (see Table A.1 for model parameters). For the identified components (colored symbols), the error bars show the systematic errors, which are defined as $0.5 \times b_{maj}$ for resolved components. For unresolved components, the resolution limit is used (Kovalev et al. 2005). A linear regression fit to associated components is shown. Components not included in the fit are shown in gray. We note, in particular, the components in the region of the "tuning fork" are excluded since the region is too complex. The mean apparent speed is determined for components J3 to J10.

Fig. 5. Time evolution of Cen A at 8.4 GHz. Contour clean images, restored with a common beam of (3.33×0.78) mas at PA = $26.3°$. The contours indicate the flux density level, scaled logarithmically, and increased by a factor of 2, with the lowest level set to the 5σ-noise-level. The positions and FWHMs of the Gaussian `modelfit` components are overlaid as black circles (for model parameters see Table A.1).

4.1. Overall jet structure and flow

Our observations of Cen A reveal a complex jet flow with a wide range of individual component velocities (Sect. 3.3). Although a significant component motion is measured, the observed features in the space-VLBI image of 2000 (Horiuchi et al. 2006) show that the basic jet structure is stable over years, forming a well-confined channel. The median apparent speed then may be associated with the underlying flow that follows this preformed jet structure. At the same time, owing to the interaction between the jet and the ambient medium, individual jet features are developed that can be slower or even stationary.
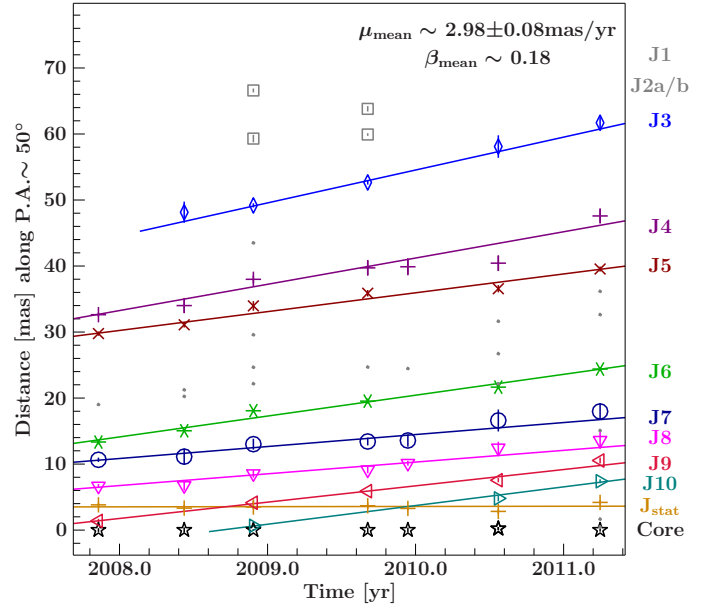
As shown by the tapered analysis, the TANAMI observations resolve the substructure of prominent regions into components of a few light days in size. Tingay et al. (2001) reported some dramatic flux variability of components without major changes in apparent speed, which already hinted at a finer substructure.

We measured a position-dependent acceleration (see Fig. 8) of the outer components (beyond ~0.3 pc), which is very similar to the velocity distribution seen in the subparsec region of NGC 1052 (see Fig. 13 in Lister et al. 2013). If one assumes that the acceleration continues downstream, it could be the explanation for the apparent mismatch in jet velocity at a distance of ~100 pc (~0.5c; Hardcastle et al. 2003) and the parsec-scale velocities measured by VLBI (Tingay et al. 2001, and this work). However, when assuming the measured acceleration continues downstream, the jet flow already reaches a speed of $\beta_{app} \sim 0.5$ at a distance of ~2.5 pc. Alternatively, jet bending within the inner few parsecs could also explain the observed apparent acceleration. Tingay et al. (1998) constrained the angle to the line of sight on parsec scales to $50°$–$80°$, while the analysis at ~100 pc by Hardcastle et al. (2003) resulted in ~$15°$.

TANAMI observations yield surface brightness jet-to-counterjet ratios of $R = 4$ and $R = 7$, using the two observations with the best-sampled (u, v)-coverage of 2008 November 27 and 2011 April 1, respectively, and excluding core emission between -2 mas $< \text{RA}_{relative} < 2$ mas to account for possible absorption effects (Paper I; Tingay & Murphy 2001). The stacked image yields $R = 5$. Figure 9 shows the resulting constraints on the angle to the line of sight θ and the intrinsic speed β. For an optically thin ($\alpha = -1$), smooth jet we use

$$R = \left(\frac{1 + \beta \cos(\theta)}{1 - \beta \cos(\theta)} \right)^{2-\alpha} \tag{2}$$
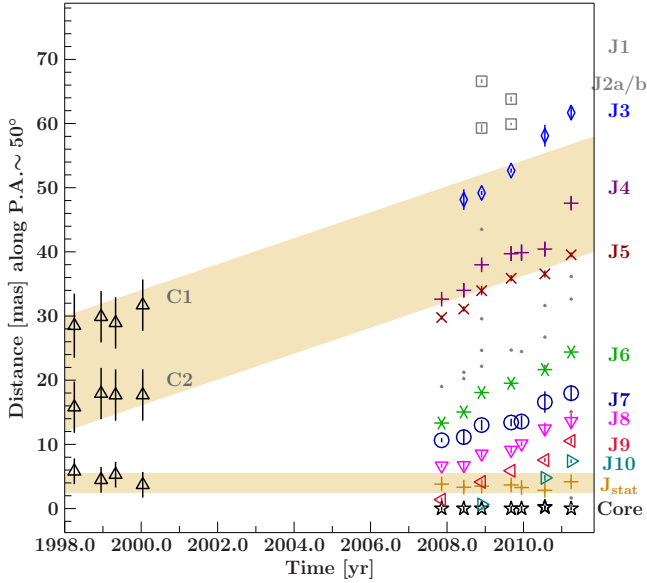
Fig. 7. 8.4 GHz kinematic results of Cen A by Tingay et al. (2001; open triangles) and the 2007–2011 TANAMI data. The shaded region marks the expected velocity evolution using $\mu = 2\,\mathrm{mas\,yr^{-1}}$, which is comparable to the mean apparent speed given by the tapered TANAMI images (see text for details).
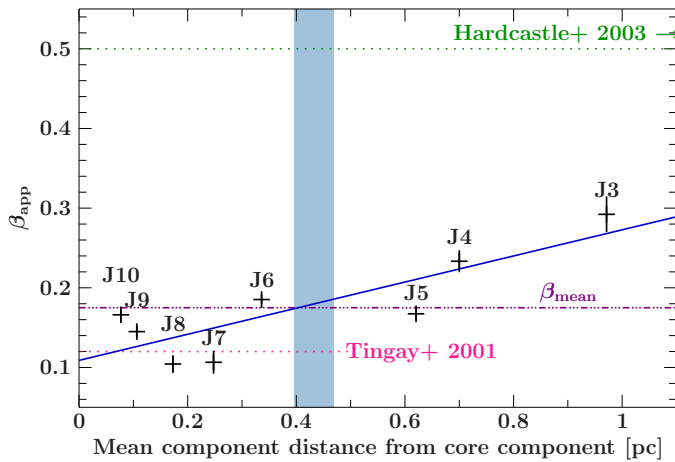

Fig. 8. Evolution of individual component velocities as a function of mean component distance from the core component, which can be parameterized by a linear fit of $\beta_{\mathrm{app}} = 0.16\,d + 0.11$ (blue line). The blue shaded area marks the position and extent of the jet widening (Sect. 4). The mean component speed and archival measurements by Tingay et al. (2001) and Hardcastle et al. (2003) are indicated by straight lines.

to constrain these parameters. The measured brightness ratio, in combination with the minimum and maximum measured proper motion, limits the jet angle to the line of sight to $\theta \sim 12°-45°$. Additionally, we can constrain the intrinsic speed to $\beta \sim 0.24-0.37$, which is comparable to measurements for NGC 1052 ($\beta = 0.25$, Vermeulen et al. 2003).

Within the uncertainties, the upper limit of our derived angles is consistent with the lower limits obtained by Jones et al. (1996) and Tingay et al. (1998), while our lower limit overlaps with the values by Hardcastle et al. (2003). These authors explained the discrepancy in measured apparent speed between the parsec and the kilo-parsec scale jet via a resolution effect and point out that Tingay et al. (1998) found hints of faster moving subcomponents. Down to scales of about ten light days, we can
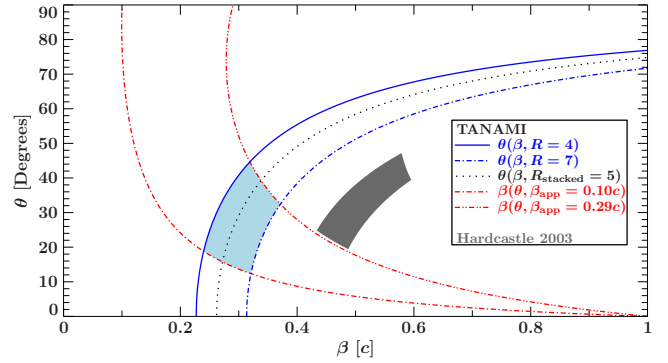
Fig. 9. Constraints on the values of the intrinsic jet speed β and the angle to the line of sight θ consistent with our measurements. Blue lines show the constraints on the θ-range for the measured jet-to-counterjet ratio. The black-dotted curve gives the corresponding values for the stacked image. The red lines give the constraints on intrinsic jet speeds based on the measured apparent speeds of the slowest and fastest component (see Table 2). The blue-shaded intersection area marks the region of permitted parameter space for both values. The gray-shaded region indicates the constraints according to measurements by Hardcastle et al. (2003).

exclude component speeds with $\beta_{\mathrm{app}} \gtrsim 0.3$, but find indications of downstream acceleration. We find that a larger angle to the line of sight cannot solely explain the faster apparent speed measured by Hardcastle et al. (2003), but requires in addition an increase in β from $\lesssim 0.3$ to $\gtrsim 0.45$, since the angle is well below the critical angle. The higher apparent speeds on kilo-parsec scales could thus consistently be explained with intrinsic acceleration assuming a constant angle to the line of sight.

The spectral index distribution of the inner few light days of the jet shows an optically thick core region with a steepening of the spectrum downstream (Paper I). It is striking that the region of the faster-moving components (J5 to J3) coincides with the optically thin region of the jet. A spine-sheath like jet-structure (e.g., Laing et al. 1999; Ghisellini et al. 2005; Tavecchio & Ghisellini 2008) could explain this whole appearance, since a faster spine at small optical depth would be revealed. For optically thick regions, only the outer – slower – layer could be probed. Further high-resolution spectral index imaging is required, however, to confirm that coincidence. A stratified jet structure can also explain the different results on the angle to the line of sight of Cen A at parsec and kilo-parsec scales. Observations of optically thin jet regions allow us to address the faster and brighter spine, resulting in higher brightness ratios, hence smaller estimated angles to the line of sight. We conclude that the different measurements of the angle to the line of sight can be better reconciled by assuming a spine-sheath structure, with possible intrinsic acceleration, rather than a large jet bending within 100 pc.

In principle, the observed downstream acceleration could also be explained via an expansion of a hot jet in pressure equilibrium with the ambient medium. If the ambient pressure has a steep density gradient, the jet expands adiabatically and accelerates (Perucho & Martí 2007). In this scenario, standing, conical (recollimation) shocks are expected to develop, though our observations do not conclusively show such features (see Sects. 4.2 and 4.3).

4.2. The stationary component J_{stat}

At a distance of $\sim$3.5 mas, the second brightest jet component J_{stat} is found to be stationary, has an almost constant

brightness temperature, and is clearly resolved from the core (Table A.1). The spectral index of J_{stat} is $\alpha \approx -1$, i.e., optically thin (Paper I). Tingay et al. (2001) discussed the appearance of a stationary component (C3) approximately at 4 mas in mid-1993 with a weakly variable flux density of about 1 Jy (for a beam size of about (3×13) mas). This result suggests that J_{stat} is a long-term stable feature. Stationary components in extragalactic jets are often observed and can be explained by locally beamed emission or standing shocks (e.g., Piner et al. 2007; Jorstad et al. 2001c; Lister et al. 2009; Agudo et al. 2012). The alternative interpretation, a large jet bending at this position (Fujisawa et al. 2000), had already been rejected by Tingay et al. (2001), as the position angles of the modelfit-components are all found to be similar. We confirm this rejection based on our even higher resolution images.

We also note that while J9 and J10 pass through J_{stat}, neither of them shows significant evidence of interactions, e.g., a flux change[3]. A possible interpretation of J_{stat} is that it represents a cross-shock in the jet flow as seen in simulations of overpressured jets (Mimica et al. 2009). In these features a spectral inversion is expected, which is associated with recollimation shocks, in which passing components are accelerated in the following expansion. To confirm J_{stat} as such, a recollimation shock will require further dual-frequency monitoring. Given the measured steep spectrum, it is more likely that this feature is the result of an internal, local pressure enhancement increasing the density and emission, similar to a jet nozzle.

4.3. The jet widening – the "tuning fork"

The "tuning fork"-like structure at $\sim 25.5 \pm 2.0$ mas (projected distance ~ 0.4 pc) downstream is significantly detected in multiple 8.4 GHz TANAMI observations and is most prominently seen in the highest dynamic range images. The dip in the surface brightness remains stationary, and the local jet morphology indicates a circumfluent behavior (Fig. 5). According to this result, we can conclude that we do not observe a moving disturbance of the jet that is caused by a temporal disruption with subsequent restructuring of the jet, but that this feature is likely a standing discontinuity.

Tingay et al. (1998) measured a strong increase in flux density of component C1 when it reached the location of the "tuning fork". The positional uncertainties of these previous VLBI measurements are not comparable to our results but their Gaussian modelfits indicated an increase in the diameter of C1 from ~ 4 mas to ~ 14 mas within ~ 3.5 months. Tingay et al. (2001) reported on no strong variations in the subsequent component C2; however, it did not reach this location during their monitoring. We therefore conclude that the jet widening might be a long-term stable feature such as J_{stat}.

At first glance the appearance of the "tuning fork" resembles a recollimation shock creating a Mach disk that decelerates the jet flow and separates it into two faster streams surrounding the central Mach disk, as seen in simulations by Perucho & Martí (2007). In between this "tuning fork" emission zone, i.e., behind the shock, one expects optically thick emission and subsequent acceleration of the jet flow. While such a recollimation shock scenario could describe the position-dependent acceleration in the succeeding components J5 to J3, the overall appearance of the structure is difficult to reconcile with the theoretical expectations, because when a Mach disk is formed, one expects a strong

jet expansion prior to the shock. Additionally, after the Mach disk, the jet should undergo further strong reconfinement shocks and be strongly decelerated. Observations show, however, that it is still well collimated and not slowing down up to a hundred parsecs (Hardcastle et al. 2003; Goodger et al. 2010). Finally, a recollimation shock would also create a bright standing feature downstream of the Mach disk, which is not observed. Thus, we can conclude the "tuning fork" is probably not caused by a recollimation shock.

A different explanation of the feature is a standing, local disturbance that does not disrupt the entire jet, such as an interaction with a massive object. Figure 3 shows that the jet surface brightness sharply increases behind the gap and starts to decline again downstream. This already suggests that the jet flow is probably intermittent but not totally stopped. In particular, we consider the penetration of a cloud or a star, which is highly likely in the inner parsec of the galaxy with estimated stellar number densities of thousands per cubic-parsec close to the galactic center (e.g., Lauer et al. 1992; Bednarek & Protheroe 1997). Following the argument in Araudo et al. (2013), the number of red giant stars inside the volume covered by the inner-parsec of the Cen A jet can be roughly estimated: using a jet diameter of 0.1 pc, an accretion rate of 0.01 L_{edd}, a stellar life time of ~ 1 Gyr, and a black hole mass of 5.5×10^7 $M_\odot$ (Neumayer 2010), one obtains on the order of 10^2 low-mass stars ($\lesssim 8$ $M_\odot$) inside the the inner-parsec of the jet. It appears reasonable that a fraction of $\lesssim 1\%$ of those might be in the red-giant phase and interacting with the jet during the TANAMI monitoring period. The exact numbers in these estimations, however, strongly depend on the stellar population, the initial mass function, and the star-forming history and are not well constrained for the inner parsec (see, e.g., Soria et al. 1996; Harris et al. 1999; Rejkuba et al. 2001, 2004, 2011, for observations and simulations of the recent star formation history and stellar population in the halo of Cen A). For further comparison, observations of Sgr A* show stars orbiting the SMBH at a distance of ~ 15 light days (Schödel et al. 2002). Since Cen A hosts a SMBH at its center that is about ten times more massive than the one in the Galaxy, we can expect stars or dust clumps orbiting the central engine down to distances of at least a few hundred light days. The distance of the "tuning fork" matches this expected range, with ~ 25 mas corresponding to ~ 600 light days.

Simulations by Bosch-Ramon et al. (2012) describe the interaction of a jet and a cloud or star orbiting the center of the AGN in the context of the formation of high-energy flaring events (Bednarek & Protheroe 1997; Barkov et al. 2010; Khangulyan et al. 2013). Such an interaction scenario between Cen A's jet and stars of the galaxy has already been discussed by Hardcastle et al. (2003), Tingay & Lenc (2009), and Goodger et al. (2010) to explain the radio and X-ray knots in the hundred-parsec scale jet. The presence of a dusty torus-like structure in the vicinity of the central black hole in Cen A is confirmed by measurements in the infrared and X-rays. Rivers et al. (2011) report an occultation event observed during twelve years of X-ray monitoring with *RXTE* at a distance commensurate with the molecular torus whose properties have been adopted from IR measurements by Meisenheimer et al. (2007). These measurements confine the dust torus to a maximum extension of ~ 0.6 pc (~ 700 light days) with an orientation axis aligned with the jet axis, also matching the distance of the jet widening from the jet core.

Interpreting the "tuning fork" as a stellar bow-shock structure due to jet-star/cloud interaction, the VLBI observations constrain its size to about $D_{bowshock} \simeq 0.5$ mas $\simeq 0.01$ pc, with a jet

---

[3] However, due to the TANAMI observation cadence, a short-time flux change might have been missed by our observations.

diameter of $R_{\text{jet}} \simeq 5\,\text{mas} \simeq 0.1\,\text{pc}$. The jet crossing time for such an object orbiting the center of Cen A with $v \simeq 10^4\,\text{km s}^{-1}$ (a typical galactic rotation velocity, see Araudo et al. 2010) is given by

$$t_j \simeq 6.2 \times 10^8 \left(\frac{R_j}{3.1 \times 10^{17}\,\text{cm}}\right) \left(\frac{v_c}{10^9\,\text{cm s}^{-1}}\right)^{-1}\,\text{s}, \qquad (3)$$

which is approximately 20 years. Assuming that the very middle of the interaction process is in 2009 2010, where our VLBI images show that the obstacle is clearly surrounded by the jet, we can thus set 1995–2005 as the decade in which the obstacle started entering into the jet. This point in time is consistent with the end of monitoring by Tingay et al. (2001). Their low-resolution images might indicate such a feature. The 3D simulations of a star or stellar wind region entering a relativistic jet (Perucho & Bosch Ramon, in prep.) show that even when the obstacle starts to enter the jet, part of the jet flow will already surround it on the outer side of the obstacle, resulting in the circumfluent behavior observed in the VLBI images.

Taking into account that the size of the shocked region ($D_{\text{bowshock}} \simeq 0.5\,\text{mas} \simeq 0.01\,\text{pc}$) can be several times the size of the obstacle (Bosch-Ramon et al. 2012), the size of the obstacle can be estimated to be about $0.1 D_{\text{bowshock}}$, i.e., $D_{\text{obstacle}} \simeq 10^{-3}\,\text{pc} \sim 200\,\text{AU}$.

With calculations by Araudo et al. (2010, Eq. (4)), we can determine a lower limit on the cloud density[4] of $n_{\text{cloud}} \geq 1.5 \times 10^{10}\,\text{cm}^{-3}$ (for more detailed calculations see Appendix A), which is three magnitudes higher than the values obtained for Cen A by Rivers et al. (2011). Moreover, the determined cloud velocity of the occultation event is about one magnitude lower than the one we assumed. A hypothetical cloud with similar parameters would be disrupted within one year, and the bow-shock like structure would have disappeared if the penetration time of a shock was smaller than the jet crossing time. Such an event therefore cannot convincingly explain the persistence of the "tuning fork" structure over $\gtrsim 3.5$ years. However, a denser object like a red giant would meet the requirements, since this scenario provides expected values and is thus favored by our calculations.

The equilibrium point between the stellar wind and a relativistic jet is determined by the wind and jet ram pressure. Following Komissarov (1994, Eq. (2)),

$$R_s = 2.3 \times 10^{13} \left(\frac{\gamma_j}{5}\right)^{-1} \left(\frac{\dot{M}}{10^{-12}\,M_\odot\,\text{yr}^{-1}}\right)^{1/2}$$
$$\times \left(\frac{v_w}{10\,\text{km s}^{-1}}\right)^{1/2} \left(\frac{P_e}{10^{-10}\,\text{dyn cm}^{-2}}\right)^{-1/2}\,\text{cm}, \qquad (4)$$

where γ_j is the jet flow Lorentz factor, $\dot{M}$ the typical mass loss rate of the stellar wind of an old late type star (expected in elliptical galaxies), v_w the velocity of the wind, and P_e the external pressure, considering that the jet is close to pressure equilibrium with the ambient medium, which is a reasonable assumption in the absence of strong recollimation shocks. However, it is very difficult to give an accurate number for this parameter, so it represents a source of error in the determination of the properties of the wind.

With $R_s = 0.01\,\text{pc}$ (bow shock diameter D_{bs}) and a jet flow velocity of $0.5\,c$ (Hardcastle et al. 2003), a typical stellar wind

velocity of $v_w = 100\,\text{km s}^{-1}$ and an ambient pressure[5] of $P_e = 10^{-10}\,\text{dyn cm}^{-2}$, we obtain an estimate for the mass loss rate of the star, $\dot{M}$:

$$\dot{M} \simeq 10^{-8} \left(\frac{R_s}{3.1 \times 10^{16}\,\text{cm}}\right)^2 \left(\frac{\gamma_j}{1.15}\right)^2$$
$$\times \left(\frac{v_w}{100\,\text{km s}^{-1}}\right)^{-1} \left(\frac{P_e}{10^{-10}\,\text{dyn cm}^{-2}}\right)\,M_\odot\,\text{yr}^{-1}. \qquad (5)$$

A red giant with a stellar wind of $v_{\text{wind}} \simeq 100\,\text{km s}^{-1}$ and a mass loss of $\dot{M} \simeq 10^{-8}\,M_\odot\,\text{yr}^{-1}$ could create such an equilibrium point at $R_s = 0.01\,\text{pc}$ if the jet flow has a velocity $v_j = 0.5\,c$, preventing the approach of the jet flow to the star during the whole crossing time of the star through the jet, provided that the conditions in the wind and the jet do not change dramatically.

Regarding the possibility of an obstacle, an increase in the radio-emission of the region is expected when the interaction started. From our estimations we conclude that the onset of the interaction must have started between 1995 and 2005. High-energy emission is expected to increase when the star enters the jet[6] (Bosch-Ramon et al. 2012; Barkov et al. 2010, 2012). In Sect. 4.5 we discuss the flux density variability of Cen A in various frequency bands. In 2000/2001, an increase in emission in the radio and X-ray is observed, but a mere coincidence cannot be excluded. Araudo et al. (2010, 2013) and Barkov et al. (2010) suggest that γ-ray emission from jet-star interaction events in Cen A could be detectable. Interestingly, after analyzing four years of *Fermi*/LAT data, Sahakyan et al. (2013) report on a possible second γ-ray spectral component in the core emission of Cen A above ~4 GeV. It is a further intriguing coincidence that the very highest energy neutrino detected in three years of IceCube integration between May 2010 and May 2013 (Aartsen et al. 2014) is positionally coincident with Cen A: at a positional uncertainty of 15.9°, the offset is only 13.6°. Cen A is by far the brightest radio source in the field and one of the strongest γ-ray sources. The high-energy emission could be produced simultaneously by different processes (including hadronic interactions, which could give rise to a neutrino component), but it is difficult to disentangle them with our current data.

Alternative explanations of the "tuning fork" involving, for example, recollimation shocks or changes in the spine-sheath structure, are not completely ruled out on the basis of the reported observations. However, we conclude that the jet-star interaction scenario can explain the observations well enough and is particularly interesting from the perspective of testability. If the "tuning fork" is caused by an obstacle moving with typical rotation velocities, it should have gone through the edge of the jet in 10 to 20 years. If it is a cloud, it could be completely shocked and advected with the jet flow before that moment, depending on its properties (Araudo et al. 2010; Bosch-Ramon et al. 2012). If instead it is a star, we should expect it to cross the jet. In either case, the situation is dynamic and, as such, temporary. If the structure is generated by a stable recollimation shock or anything else, it should last longer. With ongoing VLBI monitoring we will be able to distinguish these scenarios.

---

[4] Estimations for a jet power of $L_{\text{jet}} \simeq 10^{44}\,\text{erg s}^{-1}$ (Abdo et al. 2010), a location of the cloud of 0.4 pc, a cloud shocking time of 10 years and a cloud radius $\simeq 10^{-3}\,\text{pc}$.

[5] We adopt here the values estimated at the core of the radio galaxy 3C 31 from X-ray observations (Hardcastle et al. 2002).

[6] The *CGRO*/OSSE and COMPTEL monitoring of Cen A was between 1991 and 1995 (Steinle et al. 1998). At higher energies, a 3σ-detection by EGRET was reported (Hartman et al. 1999).
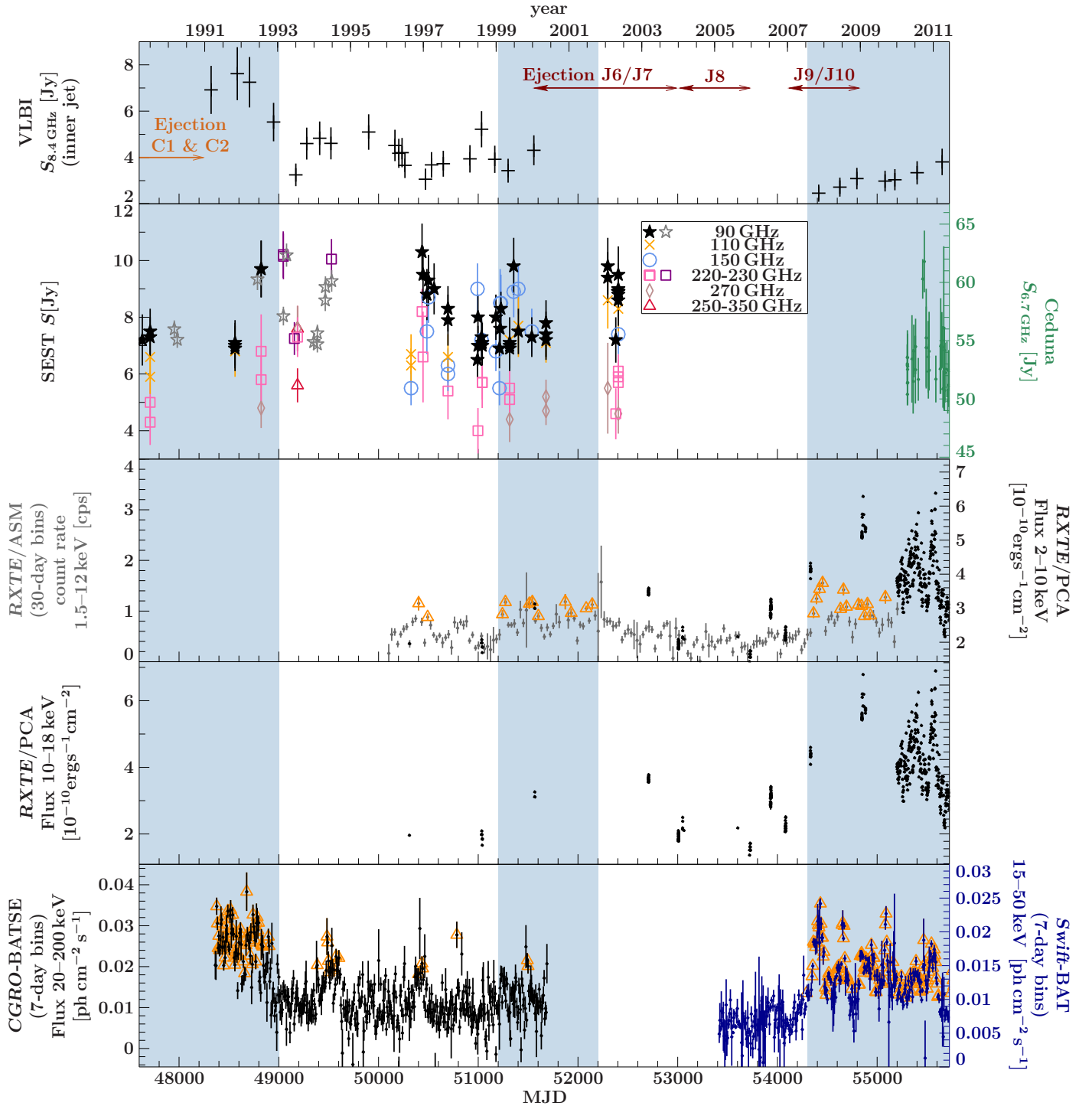
Fig. 10. Radio and X-ray light curves of the Cen A core. *From top to bottom*: archival (Tingay et al. 1998, 2001) and TANAMI 8.4 GHz flux density of inner jet ($-2\,\mathrm{mas} \lesssim \mathrm{RA}_{\mathrm{relative}} \lesssim 15\,\mathrm{mas}$) adopting an uncertainty of 15%, ejection times including uncertainties indicated by arrows (see Table 2), SEST data (90 GHz–350 GHz) from Israel et al. (2008) and Tornikoski et al. (1996), Ceduna monitoring at 6.7 GHz, *RXTE*/ASM (Data taken after MJD 55 200 are affected by an instrumental decline and were therefore excluded; see, e.g., Grinberg et al. 2013) and *RXTE*/PCA, *CGRO*/BATSE and *Swift*/BAT data after background subtraction. The blue shaded areas highlight the time periods of substantially prolonged higher X-ray activity, defined by an X-ray flux of 3σ above the mean (indicated by orange open triangles) in the continuous monitoring light curves by *RXTE*/ASM, *Swift*/BAT, and *CGRO*/BATSE.

4.4. The outer jet flow – components J5 to J3

The time evolution of the outer components J5 to J3 reveals an increase in apparent speed with distance from the core (Fig. 8). This coincides with the region where the jet becomes optically thin (Paper I). As discussed in Sect. 4.1, the better (u, v)-coverage

of the TANAMI array allows us to resolve out bright emission regions of the jet, picking up the substructure of the underlying jet flow. Assuming a spine-sheath structure of the jet, the correlation of higher speeds measured in optically thin regions could be explained consistently without claiming an internal acceleration. Furthermore, the tapered analysis of the seven TANAMI

observations of Cen A allows us to associate the prominent emission region composed of J3 and J4/J5, with the previously defined and tracked components C1 and C2 by Tingay et al. (2001). This connection is the most natural overall description of the long-term evolution of the jet.

However, as we see the position-dependent acceleration and can model a clear substructure in this outer region of the jet, other interpretation scenarios are plausible. Regardless of the nature of the jet widening – though there is most likely an interrelation – the motion of the outer components can be explained in the context of a forward shock triggering trailing components. Tingay et al. (2001) discusses C2 and C3 as trailing components of a forward shock (C1). Following this interpretation, we can directly compare the behavior of C1/C2 to J3/J4/J5.

Owing to a local perturbation in the jet, a major forward shock component can be formed followed by trailing components (Agudo et al. 2001). The simulations show an increase in velocity of the trailing components, i.e., an acceleration as function of distance up to the jet speed as a consequence of fluid expansion. That $v_{J5} \leq v_{J4} \leq v_{J3}$ fits this picture. A back extrapolation of the motion tracks of J5 and J4 gives an intersection point at ~25 mas from the core in early 2006. Trailing components of a forward shock can be easily distinguished from "normal" jet ejections, since they are not ejected from the core but created in the wake of the main perturbation (Agudo et al. 2001; Mimica et al. 2009). If J3 is a forward shock, we can constrain the jet proper motion to $v_{J5} \leq v_{jet} \lesssim 4.98 \pm 0.38$ mas yr^{-1} (see Table 2), since the flow cannot be slower than the trailing components.

As a result, J3 to J5 give a consistent picture of a forward shock and trailing components. In such a case the direct association of J3 with C1 is difficult to reconcile, since the component speeds differ significantly and internal acceleration would need to be invoked. Furthermore, the extrapolation of the tracks of C1 and C2 assuming a constant velocity of $\mu \sim 2$ mas/yr (Tingay et al. 2001) implies that the TANAMI observations should capture at least the remnants of these components at the end of the observable jet. These constraints support the more reasonable picture of the detection and association of the emerging components, but reject this proposed shock scenario. The only way to resolve this contradiction is the formation of a faster shock front (J3) on top of, passing through, and exceeding in flux density, the underlying jet flow observed by Tingay et al. (i.e., C1 and C2, 2001). This can be easily tested by future VLBI observations looking for further trailing components.

4.5. Multiwavelength variability

Cen A is a well-known high-energy emitter detected up to TeV energies (Aharonian et al. 2009) with a blazar-like broadband SED of the core emission (Abdo et al. 2010). Although intensely studied, the origin and mechanisms behind the hard X-ray emission are still under debate. The soft X-ray observations by Kraft et al. (2002) and Hardcastle et al. (2003) clearly show a contribution from the jet at kilo-parsec scales. Evans et al. (2004) suggest non-thermal X-ray emission from the parsec-scale jet. In the hard X-ray band, the situation is still ambiguous. The observed emission is similar to those in Seyfert galaxies, but it is not clear if the hard X-ray origin is also the disk or corona, as in these systems (e.g., Markowitz et al. 2007). Several results point to a jet-related spectral component, linking (jet) activity to hardening of the X-ray spectrum (Tingay et al. 1998; Fukazawa et al. 2011; Beckmann et al. 2011).

The TANAMI jet kinematics of Cen A can help constrain the emission origin of the hard X-rays further. In principle, the

correlation of a jet ejection event with an active X-ray state would indicate a similar emission origin. Tingay et al. (1998) discusses the coincidence of the ejection times of C1 and C2 with X-ray high states of Cen A, but this correlation study lacks a comparable, continuous monitoring at these higher energies.

Figure 10 compares the archival X-ray light curves of continuous monitoring by *Swift*/BAT, *RXTE*/ASM, *RXTE*/PCA, and *CGRO*/BATSE with radio monitoring with SEST at (90 GHz to 350 GHz) by Israel et al. (2008) and with the previous VLBI (Tingay et al. 2001) and TANAMI monitoring results. In the gamma rays, *Fermi*/LAT monitoring reveals Cen A as a persistent source without any flaring over more than two years (Nolan et al. 2012; Ackermann et al. 2013).

The periods of long, persistently-high X-ray states are highlighted in Fig. 10. We also show the approximate ejection times of individual radio knots. A partial overlap of the higher X-ray activity and jet-component ejection is found, although it is not significant enough to claim a common emission origin. The observation of more such correlated events are required to confirm this result. Furthermore, as discussed in Sect. 4.3, there is an indication of higher X-ray activity in 1999 and 2000 with the possible onset of the jet or obstacle interaction, though it is difficult to distinguish between the contributions of different emission mechanisms causing high energy activity.

It is, however, striking that the continuous increase in the radio flux density of the inner jet (observed with TANAMI) follows the onset of activity in hard X-rays from end of 2007 onwards, supporting the results by Fukazawa et al. (2011) and following discussions by Evans et al. (2004). The authors report on an additional power law component required to model the hard X-ray spectrum at this high activity phase, possibly due to increased jet emission. This is in contrast to spectral models describing the hard X-ray spectrum during low X-ray activity (Markowitz et al. 2007). Furthermore, note that the higher 8.4 GHz flux density in the inner jet follows the ejection of the latest components J9 and J10. The radio flux rises simultaneously with the detection of those components. As a result where the jet is becoming optically thin and when the components are detected, the total flux density increases, after the high X-ray activity. A similar correlation might be seen between the years 2001 and 2003 where the detection of J6 to J8 follows an X-ray high flux state. The SEST radio light curves from Israel et al. (2008) and Tornikoski et al. (1996) do not allow us to identify a correlated radio flare because of the sparse sampling and the large error bars.

We can conclude that there is a possible indication of a connection between hard X-ray and jet activity in Cen A. The large uncertainties in the ejection times mean that we cannot totally exclude the possibility that Cen A shows similar behavior to 3C 120 and 3C 111 where jet ejections follow a dip in the X-ray light curves (Marscher et al. 2002; Marscher 2006; Tombesi et al. 2012), which can be taken as proof of the accretion disk-jet interaction. The reported X-ray dips are shorter than the phases of lower X-ray emission seen in Cen A. Our observations point instead to jet-related hard X-ray activity than to such a direct proof of disk-jet connection. More ejection events and high-sensitivity X-ray spectra are required to confirm this result.

5. Summary and conclusions

We presented the jet evolution of Cen A at highest angular resolution ever obtained for this source, resolving and tracking up to ten individual features over ~3.5 years of less than 1 mas in size. Connecting our results with previous VLBI studies, we obtain a

consistent picture of the central pc-scale jet. The jet kinematics can be explained by a spine-sheath structure with possible intrinsic downstream acceleration. The similar appearance as a decade before (Horiuchi et al. 2006) in combination with a mean apparent speed, as previously observed for larger structures (Tingay et al. 2001), suggests an underlying jet flow that is confined within a persistent channel. Our observations clearly resolve this flow into individual jet knots. Their apparent speeds suggest a downstream acceleration that coincides with the optically thin jet.

This result connects to the findings of a faster jet at 100 pc with a spectral steepening in the outer jet regions, explainable by layers with different particle acceleration conditions (Hardcastle et al. 2003; Worrall et al. 2008). The jet-to-counterjet ratio allows us to further constrain the angle to the line of sight on parsec scales to ∼12°−45°, indicating a possible intrinsic acceleration that further connects to the faster motion detected on kilo-parsec scales.

We discussed the nature of stationary jet features, which persist within the flow. The second brightest, stationary feature at a distance of ∼3.5 mas from the core, is a long-term stable component that has lasted in the jet for more than 15 years. It is most possibly due to a locally pressure maximum, similar to a jet nozzle. Farther downstream (at ∼25.5 mas) a significant decrease in the surface brightness is detected, accompanied by a widening of the jet. This "tuning fork" structure can be explained well by the jet hitting a star. This interaction causes a local increase in the optical depth and forces the jet into a circumfluent behavior, without an entire disruption. On the basis of the reported observations, we cannot exclude the different explanation of this jet feature as a recollimation shock. However, such interaction events are expected for the denser populated central galactic region and have already been proposed to explain jet knots at several 100 pc (Hardcastle et al. 2003). It may be that such processes contribute to the γ-ray emission detected from Cen A (Abdo et al. 2010; Sahakyan et al. 2013) or could even give rise to neutrino emission. Thanks to the expected short time range of such an event, further VLBI monitoring will be able to test this scenario.

We observe a very dynamic jet with structural changes on timescales of months to years. The long-term monitoring in the X-rays reveals several relatively high flux states, prompting us to test for a correlation to phases of stronger jet activity. We can show that the onset of the higher X-ray emission end of 2007 is followed by an increase in the radio flux density of the inner jet contemporaneous with detection of two new components. A similar coincidence is indicated during active phases between 1999 and 2001 and was discussed for the activity before 1992 by Tingay et al. (1998). If such a correlation of higher (hard) X-ray flux with higher jet activity is confirmed by further VLBI monitoring, it will be a clear indication of the emission origin of hard X-rays in Cen A. As discussed by Fukazawa et al. (2011), the high hard X-ray flux phase of Cen A correlates with spectral hardening in the X-rays, possibly due to increased jet emission. The time evolution of the innermost part of Cen A in radio to X-rays could then be explained by higher jet activity causing an increase in high-energy emission. This is followed by a rise in radio brightness when these newly emerged components become optically thin. It is crucial to disentangle the emission components in the X-rays in order to better constrain the broadband spectral energy distribution of Cen A.

References

Aartsen, M. G., Abbasi, R., Abdou, Y., et al. 2013, Phys. Rev. Lett., 111, 021103
Aartsen, M. G., Ackermann, M., Adams, J., et al. 2014, Phys. Rev. Lett., 113, 101101
Abdo, A. A., Ackermann, M., Ajello, M., et al. 2010, ApJ, 719, 1433
Ackermann, M., Ajello, M., Allafort, A., et al. 2013, ApJS, 209, 34
Agudo, I., Gómez, J.-L., Martí, J.-M., et al. 2001, ApJ, 549, L183
Agudo, I., Gómez, J. L., Casadio, C., Cawthorne, T. V., & Roca-Sogorb, M. 2012, ApJ, 752, 92
Aharonian, F., Akhperjanian, A. G., Anton, G., et al. 2009, ApJ, 695, L40
Anchordoqui, L. A., Goldberg, H., & Weiler, T. J. 2001, Phys. Rev. Lett., 87, 081101
Anchordoqui, L. A., Goldberg, H., & Weiler, T. J. 2011, Phys. Rev. D, 84, 067301
Araudo, A. T., Bosch-Ramon, V., & Romero, G. E. 2010, A&A, 522, A97
Araudo, A. T., Bosch-Ramon, V., & Romero, G. E. 2013, MNRAS, 436, 3626
Barkov, M. V., Aharonian, F. A., & Bosch-Ramon, V. 2010, ApJ, 724, 1517
Barkov, M. V., Bosch-Ramon, V., & Aharonian, F. A. 2012, ApJ, 755, 170
Beckmann, V., Jean, P., Lubiński, P., Soldi, S., & Terrier, R. 2011, A&A, 531, A70
Bednarek, W., & Protheroe, R. J. 1997, MNRAS, 287, L9
Blandford, R. D., & Payne, D. G. 1982, MNRAS, 199, 883
Blandford, R. D., & Znajek, R. L. 1977, MNRAS, 179, 433
Bosch-Ramon, V., Perucho, M., & Barkov, M. V. 2012, A&A, 539, A69
Clarke, D. A., Burns, J. O., & Norman, M. L. 1992, ApJ, 395, 444
Cohen, M. H., Lister, M. L., Homan, D. C., et al. 2007, ApJ, 658, 232
Deller, A. T., Tingay, S. J., Bailes, M., & West, C. 2007, PASP, 119, 318
Deller, A. T., Brisken, W. F., Phillips, C. J., et al. 2011, PASP, 123, 275
Evans, D. A., Kraft, R. P., Worrall, D. M., et al. 2004, ApJ, 612, 786
Fanaroff, B. L., & Riley, J. M. 1974, MNRAS, 167, 31P
Feain, I. J., Cornwell, T. J., Ekers, R. D., et al. 2011, ApJ, 740, 17
Fendt, C., Porth, O., & Sheikhnezami, S. 2014, Int. J. Mod. Phys. Conf. Ser., 28, 1460190
Fujisawa, K., Inoue, M., Kobayashi, H., et al. 2000, PASJ, 52, 1021
Fukazawa, Y., Hiragi, K., Yamazaki, S., et al. 2011, ApJ, 743, 124
Ghisellini, G., Tavecchio, F., & Chiaberge, M. 2005, A&A, 432, 401
Goodger, J. L., Hardcastle, M. J., Croston, J. H., et al. 2010, ApJ, 708, 675
Greisen, E. W. 2003, Information Handling in Astronomy – Historical Vistas, 285, 109
Grinberg, V., Hell, N., Pottschmidt, K., et al. 2013, A&A, 554, A88
Hardcastle, M. J., Worrall, D. M., Birkinshaw, M., Laing, R. A., & Bridle, A. H. 2002, MNRAS, 334, 182
Hardcastle, M. J., Worrall, D. M., Kraft, R. P., et al. 2003, ApJ, 593, 169
Harris, G. L. H., Harris, W. E., & Poole, G. B. 1999, AJ, 117, 855
Harris, G. L. H., Rejkuba, M., & Harris, W. E. 2010, Proc. Astron. Soc. Aust., 27, 457
Hartman, R. C., Bertsch, D. L., Bloom, S. D., et al. 1999, ApJS, 123, 79
Homan, D. C., Kadler, M., Kellermann, K. I., et al. 2009, ApJ, 706, 1253
Honda, M. 2009, ApJ, 706, 1517
Horiuchi, S., Meier, D. L., Preston, R. A., & Tingay, S. J. 2006, PASJ, 58, 211
Houck, J. C., & Denicola, L. A. 2000, in Astronomical Data Analysis Software and Systems IX, eds. N. Manset, C. Veillet, & D. Crabtree, ASP Conf. Ser., 216, 591
IceCube Collaboration 2013, Science, 342, 1242856
Israel, F. P., Raban, D., Booth, R. S., & Rantakyrö, F. T. 2008, A&A, 483, 741
Jones, D. L., Tingay, S. J., Murphy, D. W., et al. 1996, ApJ, 466, L63

Jorstad, S. G., Marscher, A. P., Mattox, J. R., et al. 2001a, ApJ, 556, 738
Jorstad, S. G., Marscher, A. P., Mattox, J. R., et al. 2001b, ApJS, 134, 181
Jorstad, S. G., Marscher, A. P., Mattox, J. R., et al. 2001c, ApJS, 134, 181
Kellermann, K. I., Lister, M. L., Homan, D. C., et al. 2004, ApJ, 609, 539
Khangulyan, D. V., Barkov, M. V., Bosch-Ramon, V., Aharonian, F. A., &
    Dorodnitsyn, A. V. 2013, ApJ, 774, 113
Kim, H. B. 2013, ApJ, 764, 121
Komissarov, S. S. 1994, MNRAS, 266, 649
Kovalev, Y. Y., Kellermann, K. I., Lister, M. L., et al. 2005, AJ, 130, 2473
Kraft, R. P., Forman, W. R., Jones, C., et al. 2002, ApJ, 569, 54
Krauß, F., Kadler, M., Mannheim, K., et al. 2014, A&A, 566, L7
Laing, R. A., Parma, P., de Ruiter, H. R., & Fanti, R. 1999, MNRAS, 306, 513
Lauer, T. R., Faber, S. M., Currie, D. G., et al. 1992, AJ, 104, 552
Lister, M. L., Cohen, M. H., Homan, D. C., et al. 2009, AJ, 138, 1874
Lister, M. L., Aller, M. F., Aller, H. D., et al. 2013, AJ, 146, 120
Markowitz, A., Takahashi, T., Watanabe, S., et al. 2007, ApJ, 665, 209
Marscher, A. P. 2006, Astron. Nachr., 327, 217
Marscher, A. P., Jorstad, S. G., Gómez, J.-L., et al. 2002, Nature, 417, 625
McKinney, J. C. 2005, ApJ, 630, L5
McKinney, J. C., & Blandford, R. D. 2009, MNRAS, 394, L126
Meisenheimer, K., Tristram, K. R. W., Jaffe, W., et al. 2007, A&A, 471, 453
Mimica, P., Aloy, M.-A., Agudo, I., et al. 2009, ApJ, 696, 1142
Müller, C., Kadler, M., Ojha, R., et al. 2011, A&A, 530, L11
Neumayer, N. 2010, Proc. Astron. Soc. Aust., 27, 449
Nolan, P. L., Abdo, A. A., Ackermann, M., et al. 2012, ApJS, 199, 31
Ojha, R., Kadler, M., Böck, M., et al. 2010, A&A, 519, A45
Perucho, M., & Martí, J. M. 2007, MNRAS, 382, 526
Perucho, M., Hanasz, M., Martí, J.-M., & Miralles, J.-A. 2007, Phys. Ref. E, 75,
    056312
Piner, B. G., Mahmud, M., Fey, A. L., & Gospodinova, K. 2007, AJ, 133, 2357
Piner, B. G., Pushkarev, A. B., Kovalev, Y. Y., et al. 2012, ApJ, 758, 84
Rejkuba, M., Minniti, D., Silva, D. R., & Bedding, T. R. 2001, A&A, 379, 781
Rejkuba, M., Greggio, L., & Zoccali, M. 2004, A&A, 415, 915
Rejkuba, M., Harris, W. E., Greggio, L., & Harris, G. L. H. 2011, A&A, 526,
    A123
Rivers, E., Markowitz, A., & Rothschild, R. 2011, ApJ, 742, L29
Romero, G. E., Combi, J. A., Perez Bergliaffa, S. E., & Anchordoqui, L. A. 1996,
    Astropart. Phys., 5, 279
Sahakyan, N., Yang, R., Aharonian, F. A., & Rieger, F. M. 2013, ApJ, 770,
    L6
Schödel, R., Ott, T., Genzel, R., et al. 2002, Nature, 419, 694
Shepherd, M. C. 1997, in Astronomical Data Analysis Software and Systems VI,
    eds. G. Hunt, & H. Payne, ASP Conf. Proc. 125, 77
Soria, R., Mould, J. R., Watson, A. M., et al. 1996, ApJ, 465, 79
Steinle, H., Bennett, K., Bloemen, H., et al. 1998, A&A, 330, 97
Tavecchio, F., & Ghisellini, G. 2008, MNRAS, 385, L98
Tchekhovskoy, A., Narayan, R., & McKinney, J. C. 2011, MNRAS, 418, L79

Tingay, S. J., & Lenc, E. 2009, AJ, 138, 808
Tingay, S. J., & Murphy, D. W. 2001, ApJ, 546, 210
Tingay, S. J., Jauncey, D. L., Reynolds, J. E., et al. 1998, AJ, 115, 960
Tingay, S. J., Preston, R. A., & Jauncey, D. L. 2001, AJ, 122, 1697
Tombesi, F., Sambruna, R. M., Marscher, A. P., et al. 2012, MNRAS, 424, 754
Tornikoski, M., Valtaoja, E., Teraesranta, H., et al. 1996, A&AS, 116, 157
Vermeulen, R. C., Ros, E., Kellermann, K. I., et al. 2003, A&A, 401, 113
Vlahakis, N., & Königl, A. 2004, ApJ, 605, 656
Worrall, D. M., Birkinshaw, M., Kraft, R. P., et al. 2008, ApJ, 673, L135

[1] Dr. Remeis Sternwarte & ECAP, Universität Erlangen-Nürnberg,
    Sternwartstrasse 7, 96049 Bamberg, Germany
    e-mail: cornelia.mueller@sternwarte.uni-erlangen.de
[2] Institut für Theoretische Physik und Astrophysik, Universität
    Würzburg, Am Hubland, 97074 Würzburg, Germany
[3] NASA Goddard Space Flight Center, Greenbelt, MD 20771, USA
[4] CRESST/University of Maryland Baltimore County, Baltimore,
    MD 21250, USA
[5] Catholic University of America, Washington, DC 20064, USA
[6] Dept. d'Astronomia i Astrofísica, Universitat de València, 46100
    Burjassot, València, Spain
[7] Max-Planck-Institut für Radioastronomie, Auf dem Hügel 69,
    53121 Bonn, Germany
[8] Observatori Astronòmic, Universitat de València, Parc Científic,
    C. Catedrático José Beltrán 2, 46980 Paterna, València, Spain
[9] Departamento de Astronomìa Universidad de Concepción, Casilla
    160 C, Concepción, Chile
[10] CSIRO Astronomy and Space Science, ATNF, PO Box 76 Epping,
    NSW 1710, Australia
[11] Bundesamt für Kartographie und Geodäsie, 93444 Bad Kötzting,
    Germany
[12] CSIRO Astronomy and Space Science, Canberra Deep Space
    Communications Complex, PO Box 1035, Tuggeranong, ACT 2901,
    Australia
[13] School of Mathematics & Physics, University of Tasmania, Private
    Bag 37, Hobart, Tasmania 7001, Australia
[14] University of California, San Diego, Center for Astrophysics and
    Space Sciences, 9500 Gilman Dr., La Jolla, CA 92093-0424, USA
[15] Alexander von Humboldt Fellow
[16] Nordic Optical Telescope Apartado 474, 38700 Santa Cruz de
    La Palma Santa Cruz de Tenerife, Spain
[17] Hartebeesthoek Radio Astronomy Observatory, Krugersdorp, South
    Africa

Appendix A: The "tuning fork" and a possible obstacle

In Sect. 4.3 we discuss possible explanations of the jet widening ("tuning fork"), together with a decrease in surface brightness that appears to be stationary over the TANAMI monitoring period. The jet flow is likely to be disturbed by an obstacle. In the main text we conclude that a scenario including a red giant with a significant stellar wind is favored by our calculations and observations. In the following, we summarize the corresponding calculations when assuming the obstacle is a cloud.

The shock produced in the cloud by the interaction with the jet should propagate through it in a longer time than the penetration and crossing time if we expect the cloud to cross the whole jet diameter. Otherwise, the cloud would be disrupted by the shock when it has completely crossed it, and the bow-shock structure would have disappeared (Araudo et al. 2010; Bosch-Ramon et al. 2012). Knowing that the obstacle has been within the jet for at least ten years, hence a cloud shocking time of $t_{cs} > 3.1 \times 10^8$ s, we can therefore use Eq. (4) in Araudo et al. (2010) to give a lower limit of the density of the cloud:

$$t_{cs} = \frac{2 R_c}{v_{cs}} \simeq 6.2 \times 10^8 \left(\frac{R_c}{3.1 \times 10^{15}\,\text{cm}}\right)\left(\frac{n_c}{10^{10}\,\text{cm}^{-3}}\right)^{1/2}$$
$$\times \left(\frac{z}{3.1 \times 10^{18}\,\text{cm}}\right)\left(\frac{L_j}{10^{44}\,\text{erg s}^{-1}}\right)^{-1/2}\,\text{s,} \qquad (A.1)$$

where we have taken the distance to the core $z = 1\,\text{pc} = 3.1 \times 10^{18}$ cm as a reference. Taking the aforementioned lower limit on time into account and taking as input data the obstacle radius $R_c = 10^{-3}$ pc, the jet power from the literature ($L_j \simeq 10^{44}$ erg s^{-1}, Abdo et al. 2010), and the location of the "tuning fork" along the jet $z \simeq 0.4$ pc, we can give a limit on the cloud density:

$$n_c > 1.5 \times 10^{10} \left(\frac{t_{cs}}{3.1 \times 10^8\,\text{s}}\right)^2 \left(\frac{R_c}{3.1 \times 10^{15}\,\text{cm}}\right)^{-2}$$
$$\times \left(\frac{z}{1.2 \times 10^{18}\,\text{cm}}\right)^{-2}\left(\frac{L_j}{10^{44}\,\text{erg s}^{-1}}\right)\,\text{cm}^{-3}. \qquad (A.2)$$

Rivers et al. (2011) report an occultation of the central core for 170 days owing to the passage of a discrete clump of material through the line of sight in the context of a clumpy torus model. We suggest that the eclipse is short because the angular size of the eclipsed region must be small. Interestingly, for the hypothetical clump, which is located at a similar distance to the core to what is reported for the location of the "tuning fork" (0.1 . . . 0.3 pc, adopting measurements by Meisenheimer et al. 2007), they obtain a central density of $n_{clump} = (1.8-3.0) \times 10^7$ cm^{-3} and a size of $R_{clump} = (1.4-2.4) \times 10^{15}$ cm. The size of the clump would agree with our result, but the density we obtain, as required for the cloud to survive the interaction for ten years, is three orders of magnitude higher. In addition, the cloud velocity estimated by Rivers et al. (2011) is one order of magnitude lower than the one we used for our calculations ($v_{clump} \simeq 1000$ km s^{-1}, Eq. (3)). Such a decrease in the velocity would have two effects: 1.) the crossing time would be increased by a factor of ten in Eq. (3), i.e., $t_j \simeq 6.2 \times 10^9$ s (approximately two hundred years); and 2.) owing to this increase in the crossing time, the lower limit in the cloud density obtained in Eq. (A.2) would be increased by a factor of 100, bringing it to $n_c > 1.5 \times 10^{12}$ cm^{-3}. Following the result of Rivers et al. (2011), we could thus conclude that the cloud scenario should be ruled out for the "tuning fork" because: 1) it is difficult to expect clumps with higher densities at greater distances from the nucleus; and 2) the shock crossing time of the cloud, given by Eq. (A.1), would be reduced by a factor 20 with the numbers given in that paper for the cloud density, thus giving $t_{cs} \simeq 3.4 \times 10^7$ s (about one year). This means that clumps of the size and density, such as those obtained by Rivers et al. (2011) for the case of a clumpy torus, would survive for about one year before being disrupted and mixed with the jet if they come to collide with it; i.e., they would be destroyed close to the jet boundary, provided that their t_j is ∼200 years. Therefore, this scenario cannot explain the steady situation that is observed at the "tuning fork".

Table A.1. Modelfit parameters for individual jet components.

ID	S^a [Jy]	d^b [mas]	θ^b	$b_{maj}{}^c$	$\log T_B{}^d$
2007-11-10 ($\chi^2 = 5613.7$, d.o.f. $= 1954$)					
	0.01	19.69	−128.98	<0.02	>11.64
Core	0.93	0.00	–	0.58	10.69
J9	0.54	1.39	48.68	0.63	10.39
J$_{stat}$	0.61	3.82	48.31	0.68	10.37
J8	0.12	6.66	52.11	0.62	9.74
J7	0.11	10.65	44.13	0.65	9.66
J6	0.13	13.33	44.77	0.72	9.65
	0.02	19.02	45.41	<0.02	>11.64
J5	0.07	29.77	48.97	0.65	9.46
J4	0.06	32.62	50.25	0.57	9.47
2008-06-09 ($\chi^2 = 3538.4$, d.o.f. $= 3828$)					
	0.04	50.01	−128.20	2.11	8.16
	0.03	35.57	−128.05	0.49	9.33
	0.03	15.24	−130.39	<0.04	>10.99
Core	1.30	0.00	–	0.79	10.56
J$_{stat}$	0.78	3.33	46.38	0.98	10.16
J8	0.39	6.73	51.66	1.47	9.50
J7	0.23	11.12	50.16	2.41	8.85
J6	0.06	15.05	48.99	0.42	9.80
	0.09	20.25	41.72	2.47	8.40
	0.03	21.24	56.13	0.18	10.27
J5	0.07	31.10	49.03	0.82	9.25
J4	0.10	34.01	49.41	2.18	8.59
J3	0.04	48.14	52.69	3.20	7.86
2008-11-27 ($\chi^2 = 7878.1$, d.o.f. $= 7526$)					
	0.02	86.13	−128.75	0.66	8.94
	0.02	79.90	−127.60	0.77	8.81
	0.02	52.37	−129.00	0.89	8.57
	0.02	35.57	−124.72	0.35	9.45
	0.03	21.71	−126.62	0.26	9.83
	0.08	4.02	−123.25	0.54	9.70
	0.31	0.64	−118.58	<0.02	>11.82
Core	0.73	0.00	–	0.30	11.17
J10	0.56	0.64	61.92	0.39	10.82
J$_{stat}$	0.45	3.50	46.86	0.73	10.17
J9	0.24	4.14	52.20	0.54	10.16
J8	0.34	8.53	49.72	1.18	9.63
J7	0.28	13.01	49.15	1.66	9.25
J6	0.07	18.08	48.54	0.51	9.66
	0.04	22.17	42.88	0.51	9.47
	0.08	24.66	53.01	1.82	8.60
	0.11	29.58	50.56	0.85	9.41
J5	0.20	33.96	49.70	1.44	9.22
J4	0.12	37.99	49.20	1.18	9.17
	0.07	43.51	48.36	0.67	9.41
J3	0.04	49.18	51.73	0.62	9.21
J2	0.04	59.30	51.39	1.15	8.76
J1	0.03	66.59	49.68	0.60	9.10
2009-09-05 ($\chi^2 = 5250.2$, d.o.f. $= 7824$)					
	0.06	44.71	−130.13	3.85	7.83
	0.06	32.40	−125.85	3.37	7.93
	0.03	20.19	−123.59	0.14	10.47
	0.05	15.13	−124.53	0.23	10.23
	0.06	9.72	−124.34	0.56	9.56
	0.17	3.47	−114.55	0.53	10.03
Core	1.62	0.00	–	0.78	10.66
J$_{stat}$	0.68	3.67	50.77	0.95	10.11
J9	0.04	5.89	46.78	<0.03	>11.98
J8	0.37	9.12	49.06	1.03	9.79
J7	0.24	13.41	47.98	1.17	9.48
J6	0.08	19.53	48.14	0.79	9.35
	0.10	24.70	45.47	3.60	8.14
J5	0.12	35.88	49.16	0.98	9.36

Notes. All modelfit values are given without uncertainties, since they are dominated by systematics (see Sect. 3.3). $^{(a)}$ Integrated flux density of model component. $^{(b)}$ Distance and position angle of the model component from the designated phase center. $^{(c)}$ Major axis extent (FWHM) of the major axis. $^{(d)}$ Logarithm of the brightness temperature of model component.

Table A.1. continued.

ID	S [Jy]	d [mas]	θ	b_{maj}	$\log T_B$
J4	0.15	39.72	49.05	2.30	8.71
J3	0.04	52.66	50.69	0.64	9.18
J2a	0.02	59.91	49.17	0.38	9.30
J2b	0.05	63.81	49.50	0.82	9.07
	0.03	94.26	51.31	1.46	8.43
2009-12-13 ($\chi^2 = 2232.0$, d.o.f. $= 2350$)					
	0.05	45.12	−128.14	3.24	7.93
	0.09	13.72	−128.52	0.63	9.57
	0.35	3.81	−121.34	0.52	10.36
Core	1.76	0.00	–	0.72	10.77
J$_{stat}$	0.84	3.27	43.42	0.72	10.45
J8	0.31	10.11	55.31	0.74	9.99
J7	0.33	13.56	49.15	1.89	9.21
	0.12	24.47	41.03	2.67	8.48
J4	0.07	39.89	49.11	2.59	8.23
2010-07-24 ($\chi^2 = 5250.3$, d.o.f. $= 8642$)					
	0.02	68.35	−124.16	4.42	7.25
	0.07	20.74	−123.58	4.32	7.80
	0.06	9.55	−136.56	3.08	8.07
	0.06	1.21	−113.38	< 0.02	> 12.2
Core*	0.78	0.22	−44.02	0.47	10.79
Core*	0.75	0.21	135.98	0.49	10.74
J$_{stat}$	0.69	2.83	46.61	0.79	10.29
J10	0.40	4.79	43.70	0.89	9.95
J9	0.19	7.56	47.80	0.63	9.93
J8	0.26	12.43	49.88	1.92	9.08
J7	0.34	16.60	50.64	3.32	8.73
J6	0.03	21.66	46.42	0.63	9.10
	0.09	22.15	54.23	0.71	9.48
	0.11	26.72	51.16	0.70	9.59
	0.08	31.63	49.86	0.78	9.35
J5	0.12	36.57	48.39	1.12	9.23
J4	0.12	40.43	47.11	2.34	8.57
J3	0.03	58.10	53.89	3.41	7.63
2011-04-01 ($\chi^2 = 23905.7$, d.o.f. $= 6846$)					
	0.07	111.32	−126.36	3.55	7.96
	0.20	55.99	−123.57	9.71	7.56
	0.05	39.70	−124.57	0.56	9.48
	0.08	36.29	−122.40	2.89	8.20
	0.06	23.94	−124.06	0.40	9.83
	0.36	9.75	−131.91	3.45	8.73
	0.46	1.65	−127.32	0.57	10.40
	0.23	0.48	−81.91	0.04	12.41
Core	0.85	0.00	–	0.47	10.84
	0.84	1.66	44.80	0.62	10.58
J$_{stat}$	0.82	4.19	46.56	0.65	10.53
J10	0.31	7.39	49.16	0.58	10.21
J9	0.21	10.54	48.63	0.88	9.66
J8	0.23	13.60	49.24	2.50	8.82
	0.20	15.09	49.13	0.74	9.80
J7	0.21	17.97	46.48	2.50	8.76
J6	0.10	24.39	45.40	0.58	9.72
	0.06	32.64	47.70	0.57	9.53
	0.12	36.16	47.26	0.57	9.80
J5	0.14	39.54	47.53	0.75	9.64
J4	0.13	47.58	48.38	2.02	8.74
J3	0.15	61.70	48.80	2.21	8.73
	0.15	105.84	47.61	3.60	8.31

Notes. $^{(*)}$ Due to the complex structure of the core region, a stable model requires two close components which are strongly correlated. Their flux weighted central point was taken as a reference position.